Modelling of CO_2 storage in the SPE11 comparative solution benchmark

by

John Sass

to obtain the degree of Master of Science
at the Delft University of Technology,
to be defended publicly on Monday July 22, 2024 at 03:00 PM.

Student number:	5713862		
Project duration:	February 12, 2024 – July 22, 2024		
Thesis Committee:	Dr. D.V. Voskov	TU Delft	Supervisor
	Prof. Dr. H. Hajibeygi	TU Delft	Committee member
	Dr. S.C. Toby	TU Delft	Committee member
	M.B. Wapperom MSc	TU Delft	Daily supervisor

TU Delft

Abstract

This report describes the modeling decisions made to contribute to the 11th Society of Petroleum Engineers Comparative Solution Project (the 11th SPE CSP) and the conclusions from participating. The CSP includes three cases: 11A, a 2D lab-scale setup at surface conditions; 11B, an extended version of the 2D 11A geometry at reservoir conditions; and 11C, a 3D extrusion of the 11B geometry over an anticlinal-shaped curve. The impact of various modeling choices, such as gridding, discretization, and time-stepping strategies on simulation results for both surface and reservoir conditions, are discussed. Results from the 11A surface conditions case are compared to the previous FluidFlower study on which the CSP is based. A description of the DARTS framework for compositional simulation and the thermodynamic and physical properties for surface and reservoir conditions utilizing Operator-Based Linearization (OBL) is first given. Additionally, a unique approach to accurately representing injection rates that approximates and adjusts mass flux is described. The required OBL resolution to accurately capture the complex physics of the system at both surface and reservoir conditions is analyzed. Each case has a defined reporting grid size (Cartesian) prescribed by the CSP. To make quality comparisons, the models run on reporting grids of each case are used as baseline models against which all other results are compared. This includes both computing performance and simulation results. The work concludes with key takeaways, future recommendations, and the impact of the CSP on current and future CO_2 injection projects.

Acknowledgements

I am very thankful to my supervisor, Dr. Denis Voskov, for providing me with the opportunity to join the DARTS development group and work on the SPE11 benchmark project. As someone whose previous experience with reservoir simulation was limited to using commercial simulators and simple 2D models in Python, I thank Dr. Voskov for expanding my knowledge of compositional simulators such as open-darts from a developer's point of view.

I would also like to express my gratitude to my daily supervisor Michiel Wapperom. Without his guidance and advice, I would not have been able to reach this point. From deciphering poorly worded questions to solving complex issues and model behaviors, his assistance was truly critical. This is in addition to developing the immensely useful darts-flash library that was used extensively in this project.

I would also like to give my thanks to the rest of the DARTS development team for supporting me and being kind colleagues for the last five months. I would like to offer a special thanks to Dr. Aleks Novikov as he always made time to listen to my questions and help me with issues that were beyond my ability no matter how difficult or time-consuming they were.

I give my thanks to Prof. Dr. Hadi Hajibeygi and Dr. Stephan Toby for providing me with valuable feedback on this project. You both introduced interesting points that I would not have thought about before.

To all of my friends that have made studying in the Netherlands such an enjoyable experience, I look forward to the future when we can reminisce about our days of studying. The last two years have been some of the best in my life, and looking back, I know for sure that coming here was a good decision.

Finally, I thank my mother, father, and brother. In my bachelor, I was far from home but always a two hour flight away. Moving to the Netherlands in this sense was similar, but being truly isolated was new. I am grateful for your support in moving abroad now and in the future when I will be in Norway. I look forward to when I will soon see you all again in person instead of on a screen.

John Sass
Delft, July 2024

Contents

1

Introduction

The development of geologic carbon storage (GCS) systems is of the utmost importance in decreasing levels of atmospheric greenhouse gasses. In pathways modeled to limit warming to 2°C, global cumulative CO_2 stored via GCS ranges from 170-900 $GtCO_2$ over the 80-year period from 2020-2100 [Int, 2023]. In the coming decades, this will require a substantial number of new GCS projects to permanently store captured CO_2. This permanent storage depends on various trapping mechanisms that are dependent on rock and fluid characteristics. One mechanism dependent on large-scale geologic features is structural trapping where buoyant CO_2 is held in place by geologic structures similar to the trapping of oil and gas [Ajayi et al., 2019, Ringrose, 2020]. Other trapping mechanisms that are dependent on small-scale rock-fluid characteristics exist. These include residual trapping where free gas CO_2 shares pore space with brine, but is trapped due to capillary forces, dissolution trapping where CO_2 is permanently stored dissolved within the aqueous brine, and mineral trapping where CO_2 reacts with chemical species within the reservoir to form solids that are then permanently trapped [Pruess and Nordbotten, 2011, Fan et al., 2012, Delshad et al., 2013]. The mechanism that significantly enhances the dissolution trapping is CO_2 fingering. In this process, the less dense CO_2 phase rests above a more dense brine phase. At the interface between the two phases, mixing occurs due to diffusive forces. The brine at the interface dissolves CO_2 and becomes more dense. It creates instabilities where CO_2-rich brine sinks downwards and is replaced by new 'fresh' brine to create convective currents that dissolve CO_2 and transport it downwards. These dense brine columns are referred to as fingers.

The dynamic behavior of CO_2 during sequestration involves and is affected by several complex physical phenomena and properties. These include but are not limited to buoyancy-driven convective migration, the diffusion of CO_2 within brine, reservoir heterogeneity, chemical interactions, and chemical alteration of rock. Although many analytical and semi-analytical approaches exist to represent the effects of these phenomena and properties, the lack of geologically realistic input models that capture heterogeneity hinders the usefulness of these models at time scales greater than 10-100 years and actual reservoir spatial scales. It is also not feasible to represent all behaviors simultaneously at scale using analytical or semi-analytical models. Numerical modeling is key to representing these effects simultaneously at the scale of interest. However, even numerical modeling can only approximate dissolution trapping that dominates in the reservoir at longer time scales (100s to 1000s years). This poses issues as modern simulation approaches have several discrepancies between each other as seen in a benchmark study by Nordbotten et al. [2012] that suggested that even for highly idealized problems, numerical simulation tools cannot be used to model CO_2 storage with satisfactory accuracy.

Since the Nordbotten et al. [2012] benchmark, numerical simulators have seen several improvements. A more recent benchmark, the FluidFlower International Benchmark Study, attempted to reassess the predictive capabilities of numerical simulators [Flemisch et al., 2023]. The benchmark used experiments performed at lab scale and conditions [Fernø et al., 2024] as a basis for a double-blind study. This benchmark demonstrated that the convective mixing process due to density differences can be captured accurately in a qualitative sense. Quantitatively, large variations in results were observed [Flemisch et al., 2023]. Although differences in each group's numerical simulator played a role in these

variations, differences in the interpretations of each group also played a significant role. The FluidFlower benchmark did not explicitly define some structural features and constitutive properties, leaving them open to interpretation. These included modeling choices for the solubility limit of CO_2 in water, constitutive relations such as capillary pressure, and specific gridding of the domain based on an image [Nordbotten et al.]. The benchmark concluded that the observations are indicative of field-scale modeling while listing several realities that were not considered. For the soluble gas-water system at surface conditions, the benchmark found that most simulators struggled with representing surface conditions in reasonable run times due to issues with non-linear solvers [Flemisch et al., 2023].

A most recent benchmark, the 11th Society of Petroleum Engineers Comparative Solution Project (11th SPE CSP), has been organized to provide a common reference case for numerical simulation of GCS. The CSP is closely based on the Flemisch et al. [2023] benchmark and is designed to include 2D and 3D models at surface and field conditions. Within the benchmark, three cases exist: 11A, a laboratory scale 2D model that is very similar to the geometry from the Fernø et al. [2024] and Flemisch et al. [2023] studies, but with some changes, 11B, an extended version of the 2D 11A geometry at field conditions, and 11C, a 3D extrusion of the 11B geometry over an anticlinal-shaped curve at field conditions. The CSP addresses complex realities such as geologic realism (Norwegian Continental Shelf), structural heterogeneity, fluid complexities, and capillary forces. In this benchmark, no interpretation is required from participating groups. The exact geometries of reservoirs are provided by the organizers. The CSP also provides several physical and thermodynamic properties and governing equations to be used in the benchmark. The goal of this benchmark is a direct comparison of numerical simulators, not the participants' ability to interpret the benchmark description. With the inclusion of all three cases at different scales/conditions, the overall understanding of GCS storage can be greatly improved and contribute to the development of future numerical simulators and actual GCS projects.

In this report, preliminary results for the SPE11 CSP will be described. The methodology of opendarts, the numerical simulator used in this study will be described. This includes the mathematical models used, the Operator-Based Linearization (OBL) approach used to linearize systems of equations, physical and thermodynamic modeling choices, and a proposed approach to emulate injection wells. Information related to the benchmark's three cases will be described in the following chapter. Linear solvers and changes from the solvers used in the FluidFlower benchmark will be described along with an developed time-stepping strategy. The report will conclude with results for each simulation case, a discussion of the results, and a conclusion with recommendations for future GCS modeling.

2

Methodology

2.1. Mathematical Model and OBL

In this study, it is assumed that fluid flow is governed by advective-diffusive multiphase multicomponent formulation. The conservation equation for any species is written as

$$\frac{\partial}{\partial t}\left(\phi\sum_{j=1}^{n_p}\rho_j s_j x_{cj}\right)+\nabla\cdot\left(\sum_{j=1}^{n_p}x_{cj}\rho_j \boldsymbol{u}_j+s_j\rho_j\mathbf{J}_{cj}\right)+\sum_{k=1}^{n_k}v_{ck}r_k=0\quad c=1,...,n_c, \tag{2.1}$$

where ϕ is porosity, ρ_j is phase density (kmol/m^3), s_j is phase saturation, and x_{cj} is the the molar fraction of component c in phase j.

For the energy conservation equation, advective and conductive heat flow including contributions from rock and fluid are accounted for as

$$\frac{\partial}{\partial t}\left(\phi\sum_{j=1}^{n_p}\rho_j s_j U_j+(1-\phi)\,U_r\right)+\nabla\cdot\left(\sum_{j=1}^{n_p}h_j\rho_j\boldsymbol{u}_j+\kappa\nabla T\right)+\sum_{k=1}^{n_k}v_{ek}r_k=0, \tag{2.2}$$

where U_j is phase specific energy (kJ/kmol), U_r is rock specific energy (kJ/m^3), and κ is the combined heat conduction term (kJ/day/K).

The velocity $\mathbf{u}_j$ follows the multiphase flow extension of Darcy's law which includes capillary and gravitational effects as

$$\boldsymbol{u}_j=-\mathbf{K}\frac{k_{rj}}{\mu_j}\left(\nabla p_j-\boldsymbol{\gamma}_j\nabla z\right), \tag{2.3}$$

where $\mathbf{K}$ is the permeability tensor (mD), k_{rj} is the relative permeability of phase j, μ_j is the viscosity of phase j (mPa·s), p_j is the pressure of phase j (bars), $\boldsymbol{\gamma}_j=\rho_j\mathbf{g}$ is the specific weight (N/m^3) and z is the depth vector (m).

Fick's law is used to describe the diffusive flux $\mathbf{J}_{cj}$ of component c in phase j as

$$\mathbf{J}_{cj}=-\phi\mathbf{D}_{cj}\nabla x_{cj}, \tag{2.4}$$

where $\mathbf{D}_{cj}$ is the diffusion coefficient (m^2/day). Although not used in this study, the source term in the kinetic reactions is a summation over the product of reaction rate r_k (kmol/m^3/day) and stoichiometry v_{ck} of each kinetic reaction k. If applicable, the product of r_k and associated reaction heat v_{ek} can be used.

These nonlinear equations are discretized using a finite volume approach with a two-point flux approximation and upstream weighting in space. A backward Euler approximation is used for time. The result of the discretization is a system of highly nonlinear algebraic equations. The Operator-Based Linearization (OBL) approach is used to linearize this system of equations [Voskov, 2017]. In this

approach, pressure, temperature, and overall composition are used as state variables to rewrite the governing equations 2.1, 2.2 in the form of state-dependent operators.

This is done by grouping all physical properties fully defined by thermodynamic state ω which transforms the governing equations into the following form:

$$\begin{aligned} V\phi_0 \left[\alpha_c(\omega) - \alpha_c(\omega_n)\right] - \Delta t \sum_{l \in L(i)} \sum_{j=1}^{n_p} \left[\Gamma^l \beta_{cj}^l (\omega^u) \Delta\Psi_j^l + \Gamma_d^l \gamma_j^l(\omega) \Delta\chi_{cj}\right] \\ + \Delta t V \delta_c(\omega) = 0, \quad c = 1, ..., n_c, \end{aligned} \tag{2.5}$$

$$\begin{aligned} V\phi_0 \left[\alpha_{ef}(\omega) - \alpha_{ef}(\omega_n)\right] - \Delta t \sum_{l \in L(i)} \sum_{j=1}^{n_p} \left[\Gamma^l \beta_{ej}^l (\omega^u) \Delta\Psi_j^l + \Gamma_d^l \gamma_j(\omega) \Delta\chi_{ej}\right] \\ + \Delta t V \delta_e(\omega) + (1-\phi_0) V U_r \left[\alpha_{er}(\omega) - \alpha_{er}(\omega_n)\right] \\ - \Delta t \sum_l (1-\phi_0) \Gamma_d^l \kappa_r \alpha_{er}(\omega) \Delta\chi_{er} = 0, \end{aligned} \tag{2.6}$$

where each operator represents a combination of physical properties and relations from the governing system in equations 2.1 and 2.2 to capture complex physics and nonlinear terms.

The state-dependent operators are discretized in physical space within defined bounds assigned for each model. This discretization can be uniform or non-uniform. For uniform discretization, the same number of points are evenly spaced and assigned to all dimensions. In non-uniform discretization, the number of points can differ between dimensions and point distribution can be refined near certain values on each dimensional axis. In this study, the point distribution, referred to as resolution, is evenly spaced along all dimensions, but the total number of points along the pressure axis is decreased in most models.

Throughout a simulation, the operators and derivatives are evaluated by multi-linear interpolation using current state variable values. The accuracy of the solution increases when more points are used to parameterize while performance decreases as additional points must be generated [Khait and Voskov, 2017]. In both field and surface conditions, it is critical to have a sufficient OBL resolution to capture the solubility behavior of CO_2 in brine [Lyu and Voskov, 2023].

In general, a sufficient number can be assumed from experience with similar models, but to confirm this, results from varying numbers of points must be compared. At a certain resolution, the increase in accuracy is negligible when compared to the additional computational time. This resolution can then be considered to be sufficient.

2.2. Thermodynamics and Physical Modeling

In this work, a binary system of H_2O and CO_2 is used. These components are distributed between an aqueous phase with no effects of salinity and a vapor phase. To solve the system of governing equations fro thermodynamic equilibrium, a fugacity-activity model is applied in a negative flash procedure with successive substitution [Michelsen and Mollerup, 2004]. The objective function of multiphase Gibbs energy is given by

$$G^* = G/RT = \sum_{j=1}^{n_p} \sum_{i=1}^{n_c} n_{ij} \ln \hat{f}_{ij}, \tag{2.7}$$

where n_{ij} is the number of moles of species i in phase j.

The material balance for each component is given as

$$x_{i0} + \sum_{j=1}^{n_p - 1} v_j (x_{ij} - x_{i0}) = z_v \quad i = 1, ..., n_c, \tag{2.8}$$

where phase 0 is the reference phase. Mole fractions of each phase must sum to 1 which gives

$$\sum_{i=1}^{n_c} (x_{ij} - x_{i0}) = 0, \quad j = 1, ..., n_p - 1. \tag{2.9}$$

When calculating phase equilibrium, the material balance and fugacity constraints must be satisfied. The equilibrium equations as given by Michelsen and Mollerup [2004] are

$$\ln y_i - \ln x_i = \ln K_{il} = \ln \phi_i^j - \ln \phi_i^k, \quad l = 1, ..., n_p - 1. \tag{2.10}$$

Because the model utilizes successive substitution, the material balance is solved using the Rachford-Rice equation in an inner loop where fugacity coefficients are considered composition-independent, while fugacities are updated in an outer loop. This weak dependence on composition results in rapid convergence as shown in Michelsen [1982]. In this binary system, the Rachford-Rice equation is a monotonically decreasing function within the negative flash window, so the inner loop can be directly solved. To calculate fugacities for phase equilibrium, the Peng-Robinson equation of state [Peng and Robinson, 1976] is used for the vapor phase, while an activity model is used for the aqueous phase [Ziabakhsh-Ganji and Kooi, 2012].

The activity model has a direct expression in terms of pressure, temperature, and composition to solve for activity and fugacity. For the Peng-Robinson EOS, the partial derivatives of the reduced residual Helmholtz function F

$$F = \frac{A^r\left(T, V, \mathbf{n}\right)}{RT} \tag{2.11}$$

are used to calculate thermodynamic properties. In this fugacity-activity approach, the fugacity and its derivatives are given as

$$\ln \hat{\varphi}_i = \left(\frac{\partial F}{\partial n_i}\right)_{T,V} - \ln Z, \tag{2.12}$$

$$\left(\frac{\partial \ln \hat{\varphi}_i}{\partial T}\right)_{P,\mathbf{n}} = \left(\frac{\partial^2 F}{\partial T\, \partial n_i}\right)_V + \frac{1}{T} - \frac{\bar{V}_i}{RT}\left(\frac{\partial P}{\partial T}\right)_{V,\mathbf{n}}. \tag{2.13}$$

Properties directly used to capture thermal effects and phase mixing during CO_2 injection include density and enthalpy, the latter of which is given as

$$\frac{\bar{H}_i^r\left(T, P, \mathbf{n}\right)}{RT} = -T\left(\frac{\partial \ln \hat{\varphi}_i}{\partial T}\right)_{P,\mathbf{n}}. \tag{2.14}$$

Using the a and b constants from the Peng-Robinson EOS, the Helmholtz energy for n moles of a mixture is then given by

$$F = \frac{A^r\left(T, V, \mathbf{n}\right)}{RT} = -n\ln\left(1 - B/V\right) - \frac{D\left(T\right)}{RTB\left(\delta_1 - \delta_2\right)}\ln\left(\frac{1 + \delta_1 B/V}{1 + \delta_2 B/V}\right), \tag{2.15}$$

where B denotes nb_{mix} and D denotes $n^2 a_{mix}$ for mixture parameters a_{mix} and b_{mix} that replace pure component parameters a and b from EOS. Terms δ_1 and δ_2 are given as

$$\delta_1 = \frac{1}{2}\left(c + 1 + \sqrt{\left(c+1\right)^2 + 4c}\right) \tag{2.16}$$

and

$$\delta_2 = \frac{1}{2}\left(c + 1 - \sqrt{\left(c+1\right)^2 + 4c}\right). \tag{2.17}$$

The system is housed in a thermodynamic library called ”darts-flash”. The results of which can be seen in Figure 2.1 where mutual solubilities of CO_2 and H_2O, as well as density and viscosity for the CO_2 and aqueous phases can be seen ranging from surface conditions for 11A to field conditions for 11B and 11C. These properties are of critical importance to accurately represent the primary trapping mechanisms for the benchmark’s timescale. Phase compositions have direct effects on both density and viscosity, which in turn govern the migration path of the CO_2 plume. Primarily in the 11A case at surface conditions but also relevant for the field conditions of 11B and 11C, the density of CO_2 will determine the height of the column of vapor phase required to overcome the capillary entry pressure of sealing layers. For dissolution trapping, the solubility of CO_2 in water and the resulting density are

the driving factors in gravity-induced currents that result in fingering patterns. These fingers account for a majority of the CO_2 trapped via dissolution.

All properties are highly dependent on pressure and temperature except for dissolved H_2O in the CO_2-rich phase at field conditions. At high pressures, changes in pressure have little effect on solubility. This is when the CO_2 is in a dense phase. At low pressures, the CO_2 is a vapor which leads to high amounts of H_2O within the CO_2 phase. At low pressure, as pressure increases, the transition from the vapor phase to the dense phase results in a steep drop in solubility.

Other effects of CO_2 phase change can be seen in the density and viscosity curves of the CO_2-phase where sharp increases in density and viscosity can be seen at low pressures as the vapor transitions to the dense phase. These sharp increases are more pronounced at lower temperatures as CO_2 transitions into the liquid phase. At higher temperatures, this transition is to the supercritical phase which results in more gradual changes.

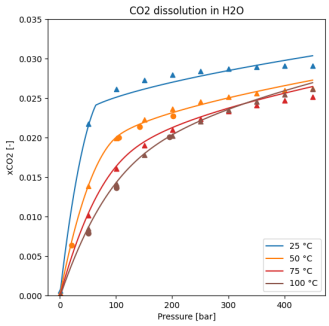

(a) CO_2 in aqueous phase

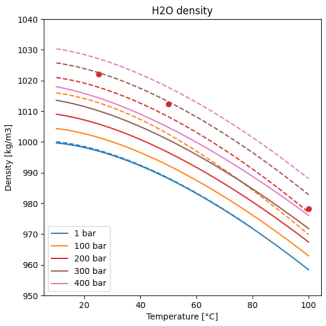

(b) Density of aqueous phase

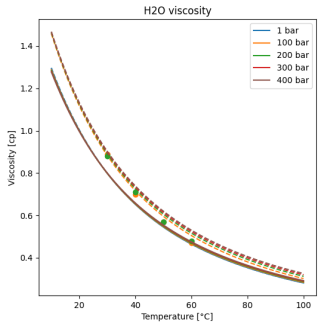

(c) Viscosity of aqueous phase

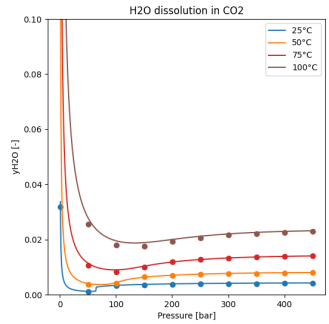

(d) H_2O in CO_2-phase

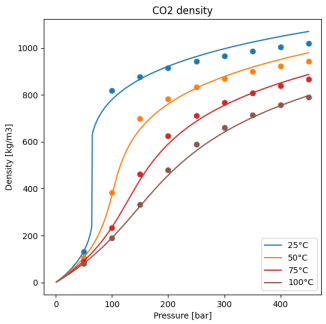

(e) Density of CO_2-phase

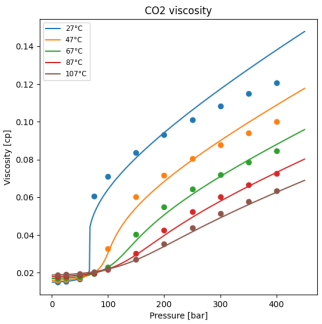

(f) Viscosity of CO_2-phase

Figure 2.1: **a** Solubility of CO_2 in the aqueous phase with data from Spycher et al. [2003] (triangle) and Koschel et al. [2006] (circle), **b** brine density where solid curves are pure phase and dashed curves show CO_2 saturated brine with data for CO_2 saturated brine from Hnědkovský et al. [1996], **c** brine viscosity where solid curves are pure phase and dashed curves show CO_2 saturated brine with reference data for CO_2-saturated brine from Bando et al. [2004], **d** solubility of brine in the CO_2-phase with data from Spycher et al. [2003], **e** CO_2-phase density with data from Lemmon et al. [2023], and **f** CO_2-phase viscosity with data from Fenghour et al. [1998].

In the reservoir conditions of the 11B and 11C cases, thermal effects are included and introduce many thermophysical interactions that must be taken into account. The formulation of enthalpy in equation 2.2 accounts for enthalpy changes as a result of these phenomena such as dissolution, evaporation, phase changes, reactions, and those related to the Joule-Thomson effect. Figure 2.2 shows the Joule-Thomson coefficient and mixing enthalpies for CO_2 and H_2O. Although the Joule-Thomson phenomenon does not play a large role in this study, it is important to validate the related effects. Similar to the density and viscosity of CO_2, the steepest change at the phase transition occurs at low pressure while increasing pressure results in a smoother drop. Additionally, accounting for enthalpy changes associated with the dissolution of CO_2 or vaporization of H_2O is critical for accurately representing phase

behavior.

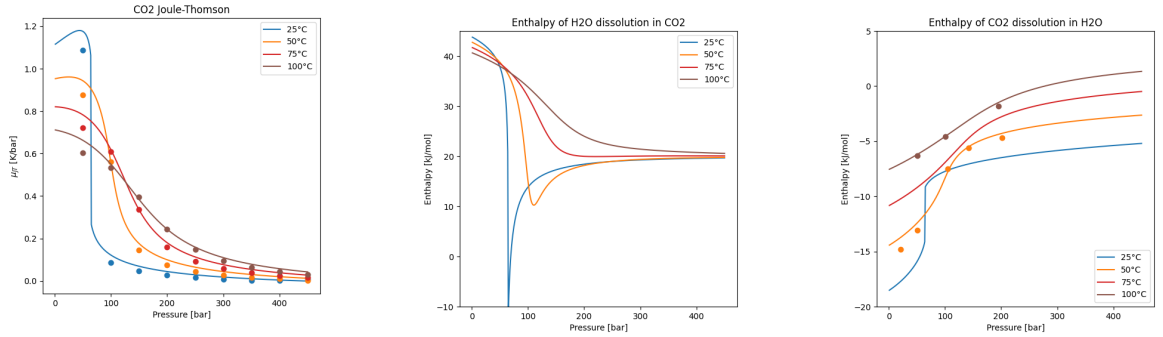

(a) Joule-Thomson coefficient for CO_2-phase

(b) Enthalpy of H_2O vaporization

(c) Enthalpy of CO_2 dissolution

Figure 2.2: Thermal properties from phase EOS: Peng and Robinson [1976] for CO_2 and Ziabakhsh-Ganji and Kooi [2012] for H_2O; **a** Joule-Thomson coefficient for CO_2-phase with data from Lemmon et al. [2023] where the Joule-Thomson coefficient can be calculated from the derivatives of the fugacity coefficient, **b** enthalpy of H_2O vaporization, and **c** enthalpy of CO_2 dissolution with data from Koschel et al. [2006].

For relative permeability and capillary pressure curves, a Brooks-Corey type model prescribed by the CSP is used. In this model, the effects of hysteresis are not considered as it was considered of lesser conceptual importance [Nordbotten et al., 2024b]. Normalized saturations are used

$$s_{w,n} = max\left(\frac{s_w - s_{w,imm}}{1 - s_{w,imm}}, 0\right) \quad \text{and} \quad s_{n,n} = max\left(\frac{s_n - s_{n,imm}}{1 - s_{n,imm}}, 0\right), \tag{2.18}$$

where $s_{a,\text{imm}}$ is the residual saturation of phase a below which the phase is immobile.

The relative permeability of a phase given as a function of saturation as

$$k_{r,a}(s_a) = (s_{a,n})^{c_{a,1}}, \tag{2.19}$$

where the $c_{a,1}$ exponent determines the non-linearity of the relative permeability curves. Figure 2.3 shows relative permeability curves for facies 5 for the 11B and 11C cases at reservoir conditions.

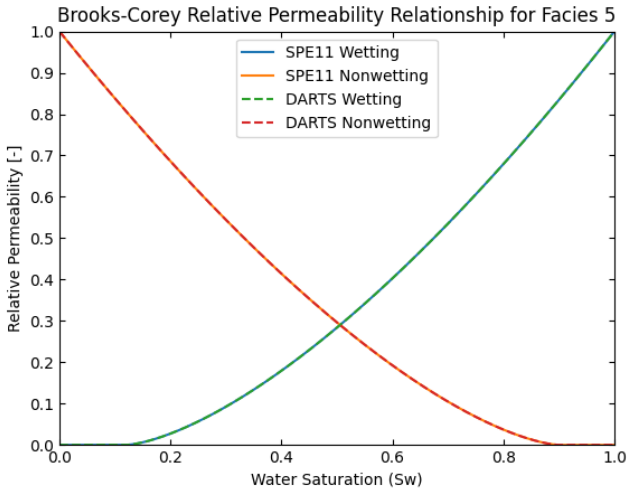

Figure 2.3: Relative permeability curves for facies 5, 11B and 11C case

For capillary pressure, the basic Brooks-Corey expression is given by

$$\widetilde{p}_{cap}(s_w) = p_{entry} \cdot (s_{w,n})^{-\frac{1}{c_2}}. \tag{2.20}$$

In this formula, p_{entry} is the entry pressure of a rock facies. In the 11A case, p_{entry} is independent of any other variables. In the 11B and 11C cases, p_{entry} is based on the Leverett J-scaling

$$p_{\text{entry}} = \sqrt{\frac{\phi}{k_x}} \cdot 6.12 \cdot 10^{-3} \frac{\text{N}}{\text{m}}, \tag{2.21}$$

where the constant of 6.12 · 10^{-3} is based on values used in core flood experiments [Abdoulghafour et al., 2020]. For the non-wetting phase of CO_2, it is possible that when the saturation is below $s_{n,imm}$, a non-wetting pressure may not exist as the phase will exist as disconnected bubbles. Although in this case, $k_{r,a}$ is zero and flow calculations are not affected, it is important to resolve the lack of non-wetting pressure for thermodynamic calculations.

An extended capillary pressure function that is valid for all saturations is given as

$$p_{cap}(s_w) = p_{cap,max} \cdot \text{erf}\left(\frac{\widetilde{p}_{cap}(s_w)}{p_{cap,max}} \frac{\sqrt{\pi}}{2}\right), \tag{2.22}$$

where $p_{\text{cap,max}}$ is a maximum capillary pressure for either surface or reservoir conditions. To create a smooth transition from the capillary pressure curves to $p_{\text{cap,max}}$, the error function is used. The capillary pressure curves from equation 2.22 for reservoir conditions in the 11B and 11C cases are shown in Figure 2.4. For the 11A case, capillary pressure at all saturations is defined by the p_{entry} value for a given facies. Using values from the curve using equation 2.22 resulted in unrealistic overpressuring of the domain.

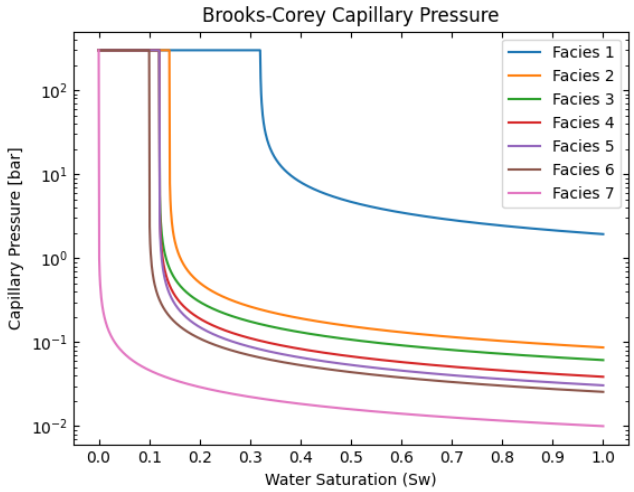

Figure 2.4: Capillary pressure for 11B and 11C reservoir conditions

In the development of density-driven fingering, gravitational instabilities at the interface between CO_2-saturated brine and pure brine are critical. These instabilities are heavily dependent on diffusion. From [Riaz et al., 2006], diffusion coefficients can be used to determine finger onset time, t_c, the time before the first finger has formed, critical wavelength, λ_c, an indication of horizontal length scales required to capture convective transport, and penetration depth of the diffusive boundary layer at the onset of instability, δ_c, a metric that is compared to total reservoir thickness to determine the validity of the model.

For the model to be valid, the penetration depth must be significantly smaller than the thickness of the reservoir. Using relationships between these two values and Rayleigh number, the constants for critical time, t_c, and critical wavenumber k_c can be used to estimate general values of onset time and critical wavelength for homogeneous, very idealized cases. These values can then be used to support decisions related to grid cell sizes. Using t_c = 146, a general estimation of onset time can be given as

$$t_c = t_c \frac{\phi \mu^2 D}{(K \Delta \rho g)^2}, \tag{2.23}$$

and using k_c = 0.07, a general estimation for critical wavelength as

$$\lambda_c = \frac{2\pi\mu\phi}{k_c K \Delta\rho_w g}, \tag{2.24}$$

and penetration depth as

$$\delta_c \approx \frac{24\mu D}{K\Delta\rho_w g}, \tag{2.25}$$

where:

- ϕ: porosity (-)
- μ: viscosity ($pa \cdot s$)
- D: diffusion coefficient (m^2/s)
- K: absolute permeability (m^2)
- $\Delta\rho$: difference in density of CO_2-saturated brine and pure brine (kg/m^3)
- g: gravity constant

Values for critical time and critical wavelength used in Riaz et al. [2006] are 146 and 0.07 for t_c and k_c respectively. However, Elenius et al. [2015] shows that usage of a capillary transition zone allows critical time to range from 31-146 with the most refined solution resulting in a value of 70 while for critical wavenumber, values ranged from 0.07 to 0.086 with the most refined solution being 0.08.

With constant diffusion assumed per phase, permeability is the largest determining factor for onset time and critical wavelength. Within the ranges of conditions in most aquifers, other properties such as viscosity and density vary little. Figures 2.5 and 2.6 show how an onset time and critical wavelength-/penetration depth depend on permeability. These figures include the possible ranges of these curves for the SPE11 conditions based on the highly idealized analytical solution.

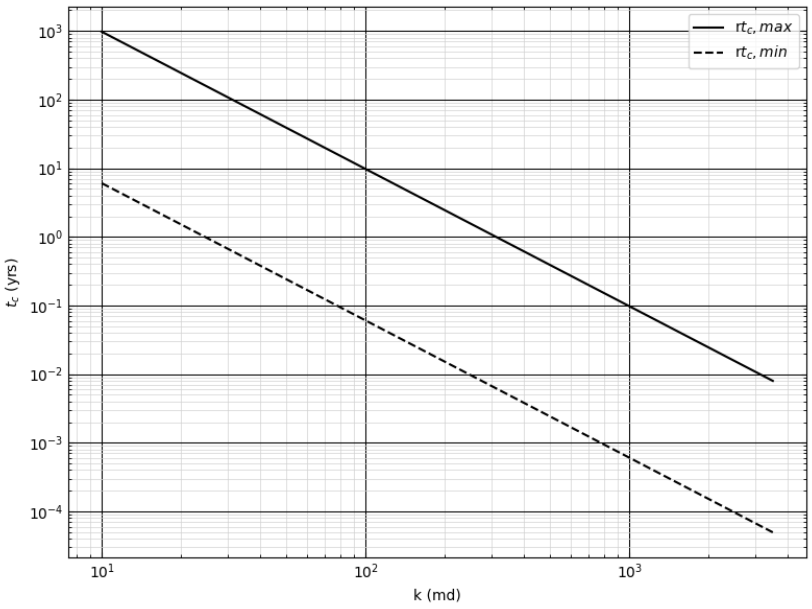

Figure 2.5: Range of possible onset times based on the formula from Riaz et al. [2006] for various permeabilities at field conditions. Ranges include maximum and minimum onset time based on ranges of constants from Elenius et al. [2015] and small ranges of possible values for viscosity and density difference.

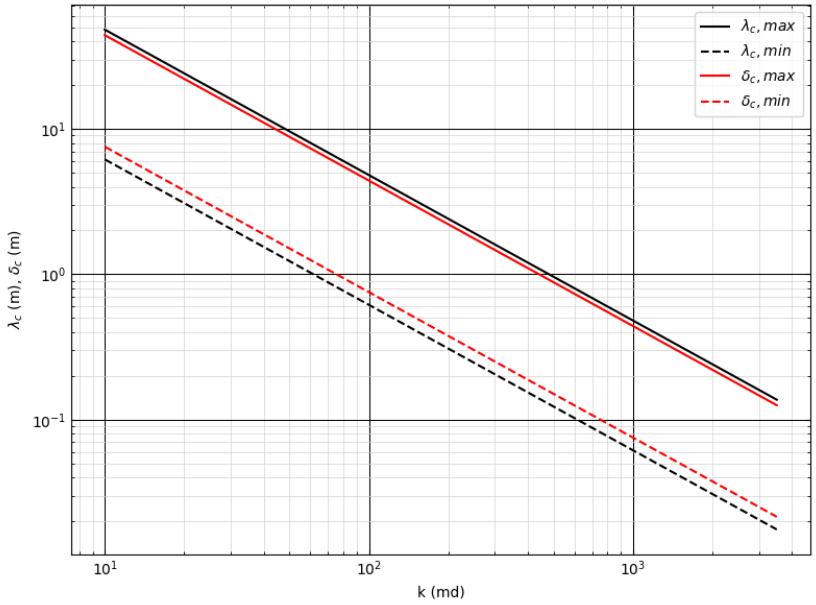

Figure 2.6: Critical wavelength and penetration depth based on Riaz et al. [2006] for various permeabilities at field conditions. Ranges include maximum and minimum onset time based on ranges of constants from Elenius et al. [2015] and small ranges of possible values for viscosity and density difference

For all properties, physical and thermodynamic properties, the CSP defines governing equations and constitutive laws. This includes many assumptions and correlations. The open-darts framework has its own set of correlations. Table 2.1 shows physical and thermodynamic properties as well as what correlations are given by the CSP and used in this study. For physical properties, this study uses the recommended sources from the CSP. This includes conductivity, relative permeability, capillary pressure, and diffusion coefficients. For properties related to thermodynamics and the numerical simulation processes of open-darts such as density, viscosity, and enthalpy, correlations for each property and phase with the inclusion of mixtures are used. The CSP assumes that mixture properties are that of the pure phase except for water density for which open-darts and the CSP both use the correlation from Garcia [2001]. Compared to the usage of pure phase properties, the inclusion of property models that account for mixtures increases the accuracy of the compositional model. With these choices, this study is in line with the goal of the CSP to compare different numerical simulators rather than groups' interpretation of the reservoir domains, geometries, and rock properties.

2.3. Mass-Rate Approximation

Wells in all three cases of CSP are defined to inject by mass rate. Wells in open-darts can set controls of pressure or volume rate. At surface, isothermal conditions, the requested mass rate can be reasonably converted to an equivalent volume rate. However, at field conditions in non-isothermal models, bottom hole pressure (BHP) can change with time. Bottom hole temperature (BHT) can also change with time, but in the 11B and 11C cases, injection temperature is fixed. It is possible to define a mass rate operator that takes pressure and temperature at the wells to calculate mass density, and then CO_2 volume based on that density. This approach was attempted but was computationally costly as properties were evaluated at every time step. As a final solution, a mass-rate approximation removes all well objects and directly adjusts the right-hand side (RHS) flux vector for cells in which wells are perforated.

In this approach, the mass rate per day (kg/day) of a well is set as the value defined by the CSP. This value is converted to mol/day of CO_2. Because this operation occurs every time step, the mole rate value is multiplied by dt to get additional moles from the previous time step. This value of moles is then added directly to the RHS flux vector. For non-isothermal models, a second step is taken. In addition to the CO_2 flux update, enthalpy flux is also updated. This is done by calculating the energy associated with the additional, injected moles of CO_2 at BHP and BHT conditions. This additional energy is then

Table 2.1: Sources for thermodynamic and physical properties used in open-darts and sources given by the SPE11 benchmark. When [Lemmon et al., 2023] is given, values used are for pure phase only. For properties where a component is not explicitly stated, properties for both components are from the same source(s)

Property	Component	open-darts	SPE11
Density	CO_2	Peng and Robinson [1976]	Lemmon et al. [2023]
	H_2O	Garcia [2001]	Garcia [2001]
Viscosity	CO_2	Fenghour et al. [1998]	Lemmon et al. [2023]
	H_2O	Islam and Carlson [2012]	Lemmon et al. [2023]
Diffusion Coefficient	-	Nordbotten et al. [2024a] & Fernø et al. [2024]	Nordbotten et al. [2024a] & Fernø et al. [2024]
Enthalpy	CO_2	Peng and Robinson [1976]	Lemmon et al. [2023]
	H_2O	Ziabakhsh-Ganji and Kooi [2012]	Lemmon et al. [2023]
Conductivity	-	Lemmon et al. [2023]	Lemmon et al. [2023]
Relative Permeability	-	Nordbotten et al. [2024a] & Fernø et al. [2024]	Nordbotten et al. [2024a] & Fernø et al. [2024]
Capillary Pressure	-	Nordbotten et al. [2024a] & Fernø et al. [2024]	Nordbotten et al. [2024a] & Fernø et al. [2024]

added to the RHS vector index for energy to account for the added CO_2.

3

Benchmark Information

3.1. Provided Information

A standard geometry was provided by the CSP to all participating groups. For meshing and grinding purposes, this information was provided in the form of a GMSH file. All other information discussed in this chapter including physical properties was provided in the CSP description from Nordbotten et al. [2024b]. This was done to remove interpretation from the benchmark to allow for direct comparisons of the capabilities of participating groups' numerical simulators. This differs from the previous Fluid-Flower benchmark which required participants to make several interpretations and decisions related to geometry as well as those related to numerical modeling.

3.2. SPE 11A

The geometry used for the 11A case is a simplified version of that described in Nordbotten et al. [2024a] and was designed to be representative of the reservoirs on the Norwegian Continental Shelf of the North Sea. The domain has a height of 1.2 m and a length of 2.8 m while maintaining a uniform thickness of 1 cm. A sketch of the geometry can be seen in Figure 3.1. The geometry contains an anticlinal structure, where CO_2 is expected to accumulate within facies 5 under facies 1, one sealing fault zone, two highly permeable fractures, two wells, and two pressure observation points. These observation points are located in the sealing layers above the injection points and provide information related to seal integrity. The setup also contains three boxes: A, B, and C, for data reporting and comparison between benchmark submissions. The coordinates of boxes, wells, and observation points can be seen as:

- Box A: Bottom left (1.1, 0.0), top right (2.8, 0.6)
- Box B: Bottom left (0.0, 0.6), top right (1.1, 1.2)
- Box C: Bottom left (1.1, 0.1), top right (2.6, 0.4)
- Well 1: (0.9, 0.3)
- Well 2: (1.7, 0.7)
- Pressure Observation Point 1: (1.5, 0.5)
- Pressure Observation Point 2: (1.7, 1.1)

The 11A model is considered isothermal at 20°C with pressure at atmospheric conditions. For boundary conditions, the left, right, and bottom boundaries are impermeable. The top boundary is considered a constant pressure boundary in contact with pure water at a pressure of 1.1 bar. The 11A model is considered isothermal at 20°C. The model is initialized as a water-filled medium at rest.

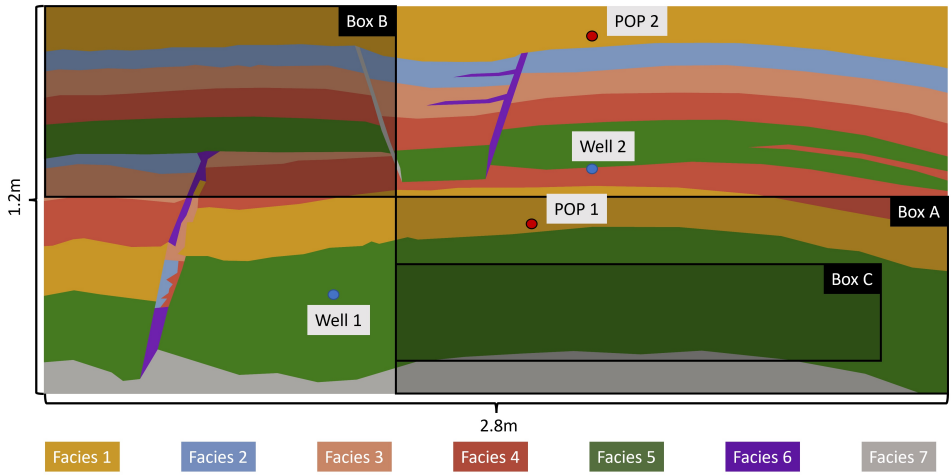

Figure 3.1: Sketch of geometry for 11A from Nordbotten et al. [2024b]

In the geometry description, there are seven facies: one representing the sealing characteristics of shale, five permeable sands, and one impermeable bedrock. Properties are consistent with those measured in laboratory setups Nordbotten et al. [2024a], Fernø et al. [2024] and can be found in Table 3.1 for properties that vary between facies, and Table 3.2 for properties that do not vary between the facies. For facies 7, permeability and porosity were set to $1 \cdot 10^{-18}$ m^2 and $1 \cdot 10^{-3}$ [-] respectively. Having non-zero values in these properties would cause issues for convergence within the model. Similarly, gas entry pressure for facies 7 was not defined in the details of the benchmark. As it is necessary to set a value for entry pressure in the model for each facies, the entry pressure for facies 7 was set to 0.1 Pa. This is the lowest value of all facies. A small value was chosen as entry pressure did not affect CO_2 entering the facies due to the very small values given for permeability and porosity. Values larger than what was assigned led to abnormally high capillary pressures within the facies, which then extended pressure outside the established OBL range. As the last undefined value, immobile wetting saturation for facies 7 was set to 0.0. As no CO_2 entered the facies, this value was irrelevant. It should be noted that setting the cells assigned to facies 7 to 'inactive' (ACTNUM = 0) is possible. This was avoided to maintain consistency with 11B and 11C which benefit from facies 7 being active for thermal boundary condition purposes.

After the model is initialized, Well 1 begins injection at t = 0. At t = 2.5 hours, Well 2 is begins injection. At t = 5 hours, both wells are shut in. This is followed by a monitoring period from t = 5 hours until t = 5 days where the flow and transport of CO_2 is monitored. Both wells inject at a rate of $1 \cdot 10^{-7}$ kg/s. At 20°C and 1.1 bar, this corresponds to a volumetric rate of ~5 cm^3 per minute.

3.3. SPE 11B

The 11B case is extruded and scaled based on the 11A case to represent reservoir conditions typical of the Norwegian continental shelf subsurface. A sketch of the 11B geometry can be seen in Figure 3.2. In the vertical direction, the reservoir is scaled to 1000 times the size of 11A (1200 m) while in the horizontal direction, the 11A model is scaled by a factor of 3000 (8400 m). To allow for three-dimensional volumes within the reservoir, thickness is increased from 1 cm to 1 m. The locations of the wells, pressure observation points, and reporting boxes have all been scaled using the same values and can be seen as:

- Box A: Bottom left (3000, 0), top right (8300, 600)
- Box B: Bottom left (100, 600), top right (3300, 1200)
- Box C: Bottom left (3300, 100), top right (7800, 400)
- Well 1: (2700, 300)
- Well 2: (5100, 700)
- Pressure Observation Point 1: (4500, 500)

Table 3.1: Properties for 11A that differ across facies

	Isotropic Intrinsic permeability ***k*** [D]	Porosity ϕ [-]	Immobile wetting phase saturation $s_{w,imm}$ [-]	Gas entry pressure p_{entry} [Pa]	Diffusion constants D_w [m^2s^{-1}]	Diffusion constants D_g [m^2s^{-1}]
Facies 1	41	0.44	0.32	1500	10^{-9}	$1.6 \cdot 10^{-5}$
Facies 2	507	0.43	0.14	300	10^{-9}	$1.6 \cdot 10^{-5}$
Facies 3	1013	0.44	0.12	100	10^{-9}	$1.6 \cdot 10^{-5}$
Facies 4	2027	0.45	0.12	25	10^{-9}	$1.6 \cdot 10^{-5}$
Facies 5	4053	0.43	0.12	10	10^{-9}	$1.6 \cdot 10^{-5}$
Facies 6	10133	0.46	0.10	1	10^{-9}	$1.6 \cdot 10^{-5}$
Facies 7	0.0	0	N/A	N/A	0	0

Table 3.2: Properties for 11A that are constant across facies

Immobile gas saturation $s_{n,imm}$ [-]	0.10
Max capillary pressure $p_{cap,max}$ [Pa]	$9.5 \cdot 10^4$
Shape exponent capillary pressure c_2 [-]	2
Shape exponent relative permeability $c_{a,1}$ [-]	2
Dispersivity E [m]	10^{-2}

- Pressure Observation Point 2: (5100, 1100)

It should be noted that the reporting boxes do not extend to the horizontal boundaries like in the 11A case. This is due to data reporting and volumetric boundary conditions that will be later discussed in further detail.

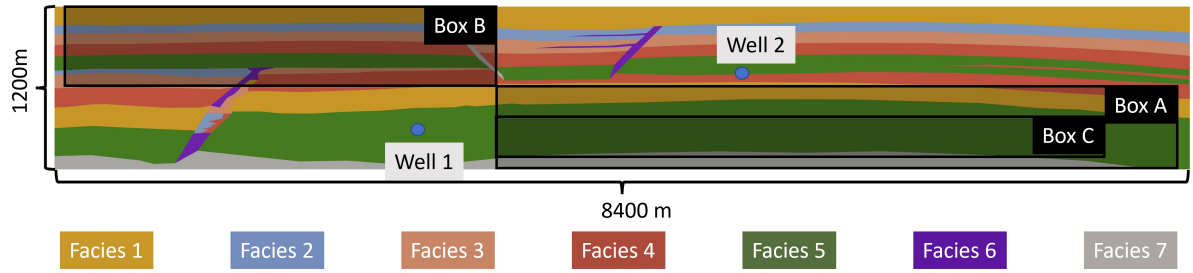

Figure 3.2: Sketch of geometry for 11B from Nordbotten et al. [2024b]

For initial and boundary conditions, it is assumed that the top of the reservoir has a depth of 2000 m. This depth is used to establish initial conditions for pressure and temperature. The temperature at the bottom of the geometry is initialized at 70°C with a thermal gradient of 25°C per 1 km in effect as:

$$s_w = 1,\ \chi_w^{H_2O} = 1,\ \mathbf{u}_a = 0 \text{ and } T(\mathbf{x}) = T_{geo}(z) \tag{3.1}$$

$$T_{geo}(\mathbf{x}) = 70 - 0.025z \tag{3.2}$$

with z being the vertical coordinate of a cell with the origin at the bottom left corner of the geometry.

Initial conditions for the model are set 1000 years before injection begins i.e. t = -1000 years. For this model, the reservoir is filled with water with temperatures assigned using the gradient in Equation 3.2. For initializing pressure, the center of Well 1 is set to a pressure of 300 bars with all other cells using

a hydrostatic gradient of 0.9775 bar per 10 m. As brine density varies slightly along the 1200 m depth of the reservoir, values of brine density from the top and bottom of the geometry, 991.74 and 1001.16 kg/m^3 were averaged to result in the used hydrostatic gradient.

This gradient is also used to regulate a temperature boundary condition along the lengths of the top and bottom boundaries. This condition exists to simulate thermal gradients from overburden and underburden layers. In this condition, temperature in cells x_B along the top and bottom boundaries are held constant according to their depths as:

$$T\left(\mathbf{x}_B\right) = T_{geo}\left(\mathbf{x}_B\right). \tag{3.3}$$

The left and right boundaries are considered to be insulating:

$$\mathbf{n} \cdot \nabla T = 0. \tag{3.4}$$

All four boundaries are considered no-flow boundaries. As previously mentioned, the 11B case includes volumetric boundary conditions in the form of modifications of pore volume. Based on the benchmark description, this modifier exists along the left and right boundaries where each boundary cell has an additional pore volume that is proportional to surface area against the boundary, ℓ, that is applied to cells based on:

- $\ell_B(x_B)$ = 5 $\cdot$ 10^{4}m for x_B on the left and right boundaries, within facies 2-5,
- $\ell_B(x_B)$ = 0m for x_B on the left and right boundaries, within facies 1 and 7,
- $\ell_B(x_B)$ = 0m for x_B on the top and bottom boundaries.

A simplification based on input conditions was made for this investigation. An additional volume, $\ell_B(x_B)$, with a value of 5 $\cdot$ 10^{4}m per m^2 of boundary surface area was used for all cells on the left and right boundaries. This includes corner cells that are on both a side and a top or bottom boundary as well as cells in facies 1 or 7 that by definition should not contain an extra volume. The result of this simplification is limited to an initial increase in the total volume of CO_2 that is within seals (facies 1). As all cells are initialized with a non-zero saturation of CO_2, a multiple-order magnitude increase in pore volume will result in a larger quantity of CO_2 in the sealing layer along the boundaries at initialization. This additional mass is not substantial (~0.83 kg) when compared to the total mass of CO_2 in sealing facies across the time of investigation where the total mass of CO_2 in all sealing layers quickly reaches values in the order of 100s of tons.

The final boundary condition is an internal boundary condition. While injecting, a well is set to a fixed temperature, 10°C. This boundary condition is applied to the cell where the well is located and is only applied while a well actively injecting as:

$$\begin{aligned} T(x_j) = T_{well} \quad &\text{if} \quad Q_j > 0 \\ \nabla T \cdot \mathbf{n} = 0 \quad &\text{if} \quad Q_j = 0. \end{aligned} \tag{3.5}$$

As the reservoir has been moved to subsurface conditions, the facies properties have been updated. Because the 11B case is a thermal model, a variety of new properties have been introduced and can be seen in Table 3.3 for properties that vary between facies and Table 3.4 for properties that are constant in all facies. Like in the 11A case, properties for facies 7 were assigned as non-zero values that mimic the impermeable, non-porous qualities of the unit. The existence of facies 7 in subsurface conditions is important for capturing the correct thermal behavior unlike in the surface condition 11A case where cells representing facies 7 could be removed while not increasing the complexity of the model.

In the 11B case, horizontal permeability utilizes the defined full facies permeability seen in Table 3.3 while a vertical anisotropy ratio defined in equation 3.6 is used for permeability in the vertical direction. This anisotropy ratio is defined by the CSP and is used by all groups participating.

$$\boldsymbol{k}(\mathbf{x}) = \begin{pmatrix} k_h(\mathbf{x}) & 0 \\ 0 & 0.1\, k_h(\mathbf{x}) \end{pmatrix}. \tag{3.6}$$

For well injection protocol, both wells are inactive during the initialization period of 1000 years. Well 1 is active from t = 0 until t = 50 years. Well 2 begins injection at t = 25 years and continues to inject until t =

Table 3.3: Properties for 11B and 11C that differ across facies

	Isotropic Intrinsic permeability ***k*** [md]	Porosity ϕ [-]	Immobile wetting phase saturation $s_{w,imm}$ [-]	Rock heat conductivity κ_s [W m^{-1}K^{-1}]	Diffusion constants D_w [m^{2}s^{-1}]	Diffusion constants D_g [m^{2}s^{-1}]
Facies 1	0.101	0.10	0.32	1.90	10^{-9}	$2 \cdot 10^{-8}$
Facies 2	101	0.20	0.14	1.25	10^{-9}	$2 \cdot 10^{-8}$
Facies 3	202	0.20	0.12	1.25	10^{-9}	$2 \cdot 10^{-8}$
Facies 4	507	0.20	0.12	1.25	10^{-9}	$2 \cdot 10^{-8}$
Facies 5	1013	0.25	0.12	0.92	10^{-9}	$2 \cdot 10^{-8}$
Facies 6	2027	0.35	0.10	0.26	10^{-9}	$2 \cdot 10^{-8}$
Facies 7	0	0	N/A	2.00	0	0

Table 3.4: Properties for 11B and 11C that are constant across facies

Immobile non-wetting saturation $s_{n,imm}$ [-]	0.10
Max capillary pressure $p_{cap,max}$ [Pa]	$3.0 \cdot 10^7$
Shape exponent capillary pressure c_2 [-]	1.5
Dispersivity E [m]	10
Rock specific heat capacity C_s [kJ kg^{-1}K^{-1}]	$8.5 \cdot 10^{-1}$
Rock density ρ_s [kg m^{-3}]	2500
Shape exponent relative permeability $c_{a,1}$ [-]	1.5

50 years. After the 50-year injection period, a monitoring period takes place until t = 1000 years. Both wells inject pure CO_2 at a constant rate set to 3024 kg/day. Actual mass rates vary during injection and are discussed in the results section.

3.4. SPE 11C

The 11C case is an arched 3-D extrusion of the 11B case. A sketch of the geometry can be seen in Figure 3.3. It utilizes the same governing equations and property values as 11B which are located in Table 3.3 and Table 3.4. To create the arched 3D structure, the 11B geometry is extended 5000 m in the Y direction along a set curve to form an anticlinal structure that is slightly tilted. At the central point in the extrusion, the geometry is elevated by 150 m.

To achieve this, the CSP has designed coordinate mapping systems for both reference and Cartesian points are used and can be seen as:

$$\begin{pmatrix} x \\ y \\ z \end{pmatrix} = \Phi(u, v, w) = \begin{pmatrix} u \\ v \\ w + 150(1 - (\frac{v-2500}{2500})^2) + \frac{v}{500} \end{pmatrix} \tag{3.7}$$

for Cartesian coordinates and as:

$$\begin{pmatrix} u \\ v \\ w \end{pmatrix} = \Psi(x, y, z) = \begin{pmatrix} x \\ y \\ z - 150(1 - (\frac{y-2500}{2500})^2) - \frac{y}{500} \end{pmatrix} \tag{3.8}$$

for reference coordinates.

Due to the change in geometry, the physical configuration of reporting boxes, pressure observation points, and wells change and can be seen as:

- Box A: Near bottom left (3300, 0, 0), far top right (8300, 5000, 750)
- Box B: Near bottom left (100, 0, 750), far top right (3300, 5000, 1350)
- Box C: Near bottom left (3300, 0, 250), far top right (7800, 5000, 550)
- Well 1: Head (2700, 1000, 300), tail (2700, 4000, 300)
- Well 2: Head (5100, 1000, 700), tail (5100, 4000, 700)
- Pressure Observation Point 1: (4500, 2500, 655)
- Pressure Observation Point 2: (5100, 2500, 1255)

A notable change is that both injection wells change from having perforations in a single cell, mimicking vertical wells, to horizontal wells that extend within the domain. Well 1 is horizontal in the Cartesian coordinate system and does not follow the curve of the reservoir extrusion. Well 2 uses the reference coordinate system. This results in the path of Well 2 following the curve of the reservoir and causes Well 2 to be slightly longer than Well 1.

For boundary conditions, additional pore volumes have been added to the front and back boundaries in addition to the left and right boundaries. The same scaling in factor $\ell_B(x_B)$ = 5 $\cdot$ 10^4m is used on all boundaries. For the top and bottom boundaries, the same temperature boundary condition as 11B is used according to equation 3.2. As the depth of the top and bottom boundaries changes across the domain, the temperature assigned to each cell changes along the curve of the reservoir arch. This results in temperature differences of nearly 4° at the peak of the arch versus the near edge of the reservoir. The well temperature boundary condition is also used from 11B to ensure that well cells have a fixed temperature of 10°C during injection. This applies to all cells along the horizontal wells.

Due to the introduction of a third dimension, permeability anisotropy defined by the CSP is updated for 11C. It is defined in the reference coordinate system as:

$$\widehat{\mathbf{k}}(\mathbf{u}) = \begin{pmatrix} k_h(\mathbf{u}) & 0 & 0 \\ 0 & k_h(\mathbf{u}) & 0 \\ 0 & 0 & 0.1\, k_h(\mathbf{u}) \end{pmatrix}. \tag{3.9}$$

In the physical Cartesian coordinate system, the permeability at any point $\boldsymbol{x} = \Phi(\boldsymbol{u})$ can be given as:

$$\boldsymbol{k(x)} = \frac{1}{J(\boldsymbol{u})} \boldsymbol{F(u)} \widehat{\boldsymbol{k}}\boldsymbol{(u)} \boldsymbol{F}^T\boldsymbol{(u)}. \tag{3.10}$$

where

$$\boldsymbol{F(u)} = \nabla\Phi = \begin{pmatrix} 1 & 0 & 0 \\ 0 & 1 & 0 \\ 0 & -\frac{3}{25}\left(\frac{v-2500}{2500}\right) + \frac{1}{500} & 1 \end{pmatrix}. \tag{3.11}$$

and $J(\boldsymbol{u}) = det\,(\boldsymbol{F}(\boldsymbol{u})) = 1$. This definition ensures that along the x direction, permeability intersects layering while in the y direction, permeability follows the layering of the facies. This allows for accurate permeability characteristics of large-scale deformation and erosional surfaces to be captured Nordbotten et al. [2024b].

Before injection, the same 1000-year initialization period as 11B is used. For conditions given at t = -1000 years, pressure at the center-line of Well 1 is set as 300 bar with the same hydrostatic gradient of 0.9774 bar per 10 m and temperature for all cells is given by equation 3.2.

After the initialization period, the well injection protocol in 11C uses the same schedule as 11B where Well 1 injects for 50 years, Well 2 begins at year 25 and injects for 25 years, and an observation and monitoring period of 950 years is initiated after the end of injection. Both wells inject with a total rate of 50 kg/s at 10°C. It is assumed that this mass is equally distributed along the 3000 m of Well 1 and the 3002 m of Well 2. Although this is not realistic in practice as fluid distribution in a horizontal wellbore is not distributed evenly along the perforations, this simplification provides consistency for comparison between submissions to the benchmark. Based on the assigned rate, each well is set to inject ~1.6 Mt/y. This adds up to a total of ~118 Mt of CO_2 injected throughout the life of the field.

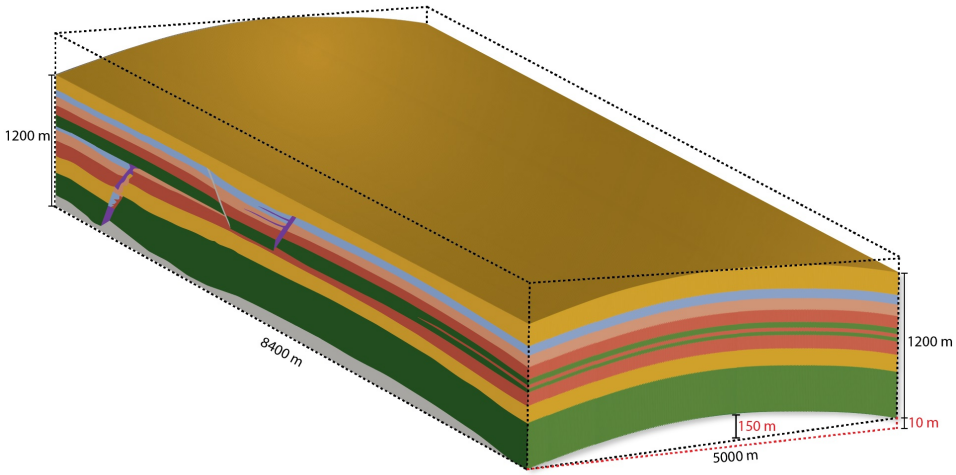

Figure 3.3: Sketch of geometry for 11C
Nordbotten et al. [2024b]

4

Solver and time-step strategies

4.1. Usage of Iterative Solvers over Direct Solvers

For the linear solutions of the systems in equations 2.1 and 2.2, open-darts can use either direct or iterative solvers, the latter of which are significantly faster for large grids like those needed to accurately capture CO_2 fingering behavior. For direct linear solvers, open-darts uses the SUPERLU library [Grigori et al., 2007]. For iterative solvers, open-darts uses the flexible generalized minimum residual (FGMRES) iterative method [Saad, 1993] to solve linear systems with a constrained pressure residual (CPR) preconditioner approach [Wallis, 1983, Wallis et al., 1985]. In the two-step CPR preconditioner, the pressure system is first decoupled from the full FIM system where a single V-cycle of the Algebraic Multigrid Method (AMG) solver is used as AMG solvers are efficient for near-elliptic problems [Stüben, 1983] like the pressure equation. In the second step, the pressure solution is used as input for an Incomplete LU factorization with 0 level of fill-in (ILU(0)) preconditioner that solves the remainder of the linear system (composition equation) as ILU(0) solvers are suited for solving near-hyperbolic equations like the composition equation [Behie and Forsyth Jr, 1983].

In this study, the default, iterative linear solvers were used. This is due to their robustness and efficiency for large models. In the FluidFlower study, issues with this system arose. The increase of linear iterations to the maximum value in the post-injection period indicated that the CPR preconditioner was failing [Wapperom et al., 2023]. This behavior was seen by most groups and was suggested to be due to the large difference between Jacobian entries in the derivatives of the conservation equations for CO_2 and brine with respect to pressure at surface conditions caused by large differences in density and viscosity [Wapperom et al., 2023]. In that study, iterative linear solvers converged well when the model was shifted to reservoir conditions.

In the SPE11 CSP, 7-th facies was changed from being the most permeable facies to being impermeable. This change has resulted in the pressure solution now converging with iterative linear solvers at surface conditions. This suggests that small numerical errors in the pressure solution grew over time within the highly permeable facies. This is a drawback of iterative solvers as numerical errors may be amplified by large coefficients proportional to permeability and force the iterative solution to fail.

4.2. Time-stepping Strategy

In conventional reservoir modeling, a simple approach is commonly used to determine time steps throughout the runtime of a model. A relatively small time step is used when solving the initial transient regime and initialization periods that may not be in equilibrium when initialized. Throughout the simulation, the time step is multiplied or divided by a chosen multiplier, often depending on the number of non-linear iterations needed to converge the solution. If the time-step exceeds an established, predefined value for the maximum desired time steps, that value of the maximum time step will be used while nonlinear iterations converge. If the solution were to converge in a high number of Newton iterations (NI) or not converge at all, this maximum time step would be cut by the multiplying factor. Several heuristics can be used to enhance the efficiency of the basic time-step strategy. For example, in the

Table 4.1: Desired change constants for pressure, saturation, and temperature

Model	Time period	η_p	η_{s_w}	η_T
11A	Injection	0.005	0.03	-
	Post-injection	0.01	0.05	-
11B	Injection	0.07	0.03	0.7
	Post-injection	0.10	0.05	1.0
11C	Injection	0.20	0.01	0.2
	Post-injection	0.50	0.03	0.5

initial FluidFlower benchmark, some heuristics related to the number of converged or non-converged nonlinear iterations within a certain reporting time were used Wapperom et al. [2023].

In this study, an approach using relative changes in properties was used to calculate an appropriate time-step multiplier for the next time-step Aziz and Settari [1979]. In this scheme, changes in pressure, saturation, and temperature were calculated for each cell in the model and were used to determine the next time-step multiplier accordingly:

$$\Delta t^{n+1} = \Delta t^n \left[\frac{(1+\omega)\,\eta_i}{\delta_i + \omega\,\eta_i} \right]_{\text{min over } i}, \tag{4.1}$$

where i refers to grid block, η_i is the specified desired change from time t^n to time t^{n+1}, δ_i is the actual change over Δt^n, and ω is a tuning factor set between 0 and 1. Values for η_i are the same for every cell but are different for each property. The values used for η_i also changed with time.

For each model, η_i values during the injection period were set to lower than those used for the post-injection period. This results in smaller time-step multipliers during the highly non-linear injection phase. These changes over time across the three models are summarized in Table 4.1. In the isothermal 11A model, only changes in pressure and saturation were used. Larger values of ω are more conservative in calculating the next time-step multiplier, while lower values of ω are more aggressive and result in larger multipliers. Because during the post-injection period, time-step size quickly reaches and consistently remains at the maximum i.e. data reporting step size, the value of ω has little to no impact in the post-injection phase. Any cut in time step is quickly remedied regardless of the ω chosen. For this reason and in all three models, a conservative ω value of 0.8 was chosen for both injection and post-injection periods with the focus of reducing the number of failed Newton iterations during the complex injection period.

5

Results

5.1. 11A Case

The 11A case was the lowest priority model in this study. That being so, attempts were made to generate results to be submitted to the CSP. Figure 5.1 shows the best results for the 11A case. In this figure, two areas with high CO_2 mole fractions can be seen. These are a lower, horizontal plume trapped just above Well 1 under the sealing facies and an area trapped under the sealing fault ~0.5 meters above Well 1. Between these two areas, trails of CO_2 that have traveled through the sealing facies are visible in the form of low, but non non-zero mole fractions of CO_2 in brine. These trails indicate that the CO_2 above this region traveled through the sealing unit until it was trapped by the sealing fault or another boundary. To the left of the fault, small amounts of CO_2 that lay just below facies boundaries are also visible. The two lower plumes of CO_2 have less CO_2 mole fraction than the two above. This is likely due to the lower permeability and higher entry pressure of the overlaying facies. These facies have not stopped all CO_2 as there is a noticeable amount of CO_2 visible just under the top boundary of the domain. This behavior is not realistic and is discussed further in Chapter 6 along with recommendations for the 11A case.

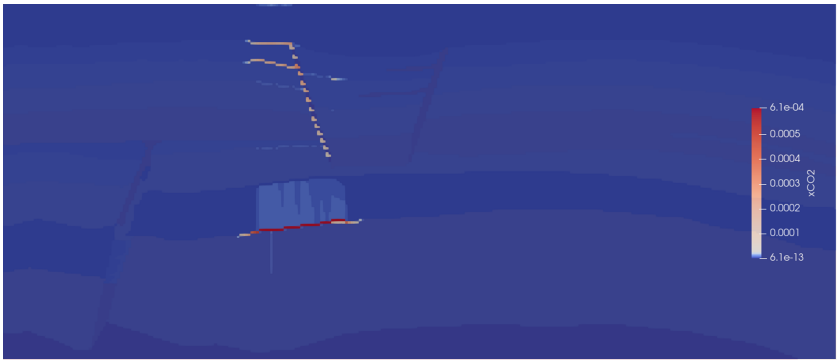

Figure 5.1: Snapshot of the 11A case 10 minutes after start of injection. CO_2 mole fraction in aqueous phase is shown with an irregular color scale to highlight diffused CO_2 vapor in the sealing facies. A semi-transparent overlay of geologic facies and their boundaries is overlaid. The grid consists of 45k cells that are 0.93 cm x 0.8 cm.

5.2. 11B Case

5.2.1. OBL Resolution

As mentioned previously, it is critical to have a sufficient OBL resolution to accurately capture CO_2 migration and enhanced dissolution in brine. However, using an excessive number of points results in unnecessary additional computation time. Figure 5.2 shows performance data for a range of OBL resolutions used for the 11B case with the reporting grid size of 100800 (10 m x 10 m) cells. This range included cases where one number of points was used for uniform discretization on all dimensions and

cases where a non-uniform discretization was used where fewer points were used for the pressure axis. All cases showed a similar number of Newton iterations with a general trend of increasing NI when more points are used. When comparing the total simulation time, the drawback of additional points is clear. With every order of magnitude increase in points, a large increase in run time is seen. It is also seen that decreasing the number of points in the pressure axis results in a decrease in run time when all other axes are held constant.

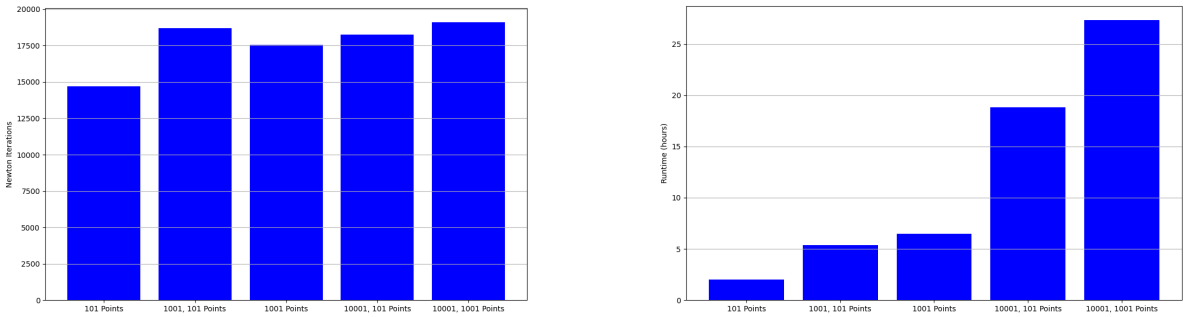

(a) Total Newton Iterations

(b) Total Simulation Time

Figure 5.2: Performance data for various OBL resolutions for the CSP reporting grid of 100800 (10 m x 10 m) cells. Curves are labeled with the number of points for all OBL axes not including pressure, and the number of points on the OBL pressure axis. For curves with only one number on the label, the number of points is the same for all OBL axes.

Using the reporting outputs defined for the CSP, it is possible to assess the quality of each result. As there is no reference case, the results must be compared and analyzed for differences. Figure 5.3 shows selected metrics based on CSP reporting criteria for box A. It is clear to see that the lowest number of points (101) is an outlier amongst the other curves, particularly in 5.3(b), and 5.3(d). In 5.3(b), the 1001-point and 10001-point uniform models show similar behavior to their corresponding models with fewer points on the pressure axis until t $\approx$ 300 years. Larger differences between these groups of curves occur after t $\approx$ 400 years. This is likely due to the onset of slightly different fingering across the models. Except for the 101-point model, all curves in 5.3(b) have similar trends. The same goes for the other three outputs in Figure 5.3. Small differences can be seen between the 1001-point and 10001-point models, but in general, all models have very similar behavior.

While time series data can give insight into the quality of results, visualizing differences in the migration of the CO_2 plume can be another method of assessing the required OBL resolution for accurate results. Figure 5.4 shows the absolute percent difference between models with 1001 and 10001 points with both models having 101 points in the pressure axis where the 10001-101 model acts as the reference case. Plume migration behavior is the primary feature to compare. When this behavior is similar between models, it can be assumed that the models are of similar accuracy. Behaviors of individual fingers are not important when looking at this type of comparison. The exact locations of fingers in numerical models are dependent on structure, heterogeneity, and numerical rounding errors, so differences in finger locations hold no weight in assessing one OBL resolution to another.

Immediately after injection ends at t = 50, the overall plume behavior of both models is very similar. The outlines of the plume entering Box B from the bottom, the plume trapped below the seal in Box A, and the plume rising above Well 2 are all visible, but the extent to which the models differ is low. At 150 years and 450 years after the end of injection, the difference in plume extent grows but is still minor. The largest differences are related to the locations of specific fingers. As mentioned previously, errors associated with fingers are of little importance. Overall, the two models are comparable in accuracy as indicated by the minute differences in plume movement.

5.2.2. Grid Resolution

In addition to OBL resolution, varying grid resolutions for the 11B case were compared. Including the CSP 11B reporting grid of 100800 (10 m x 10 m) cells, models with 50k (16 m x 12 m), 240k (7 m x 6 m), and 320k (6.25 m x 5 m) cells are compared in Figure 5.5. the resolutions can be split into low resolution models (50k and 100k) and high resolution models (240k and 320k). At t = 200 years, the

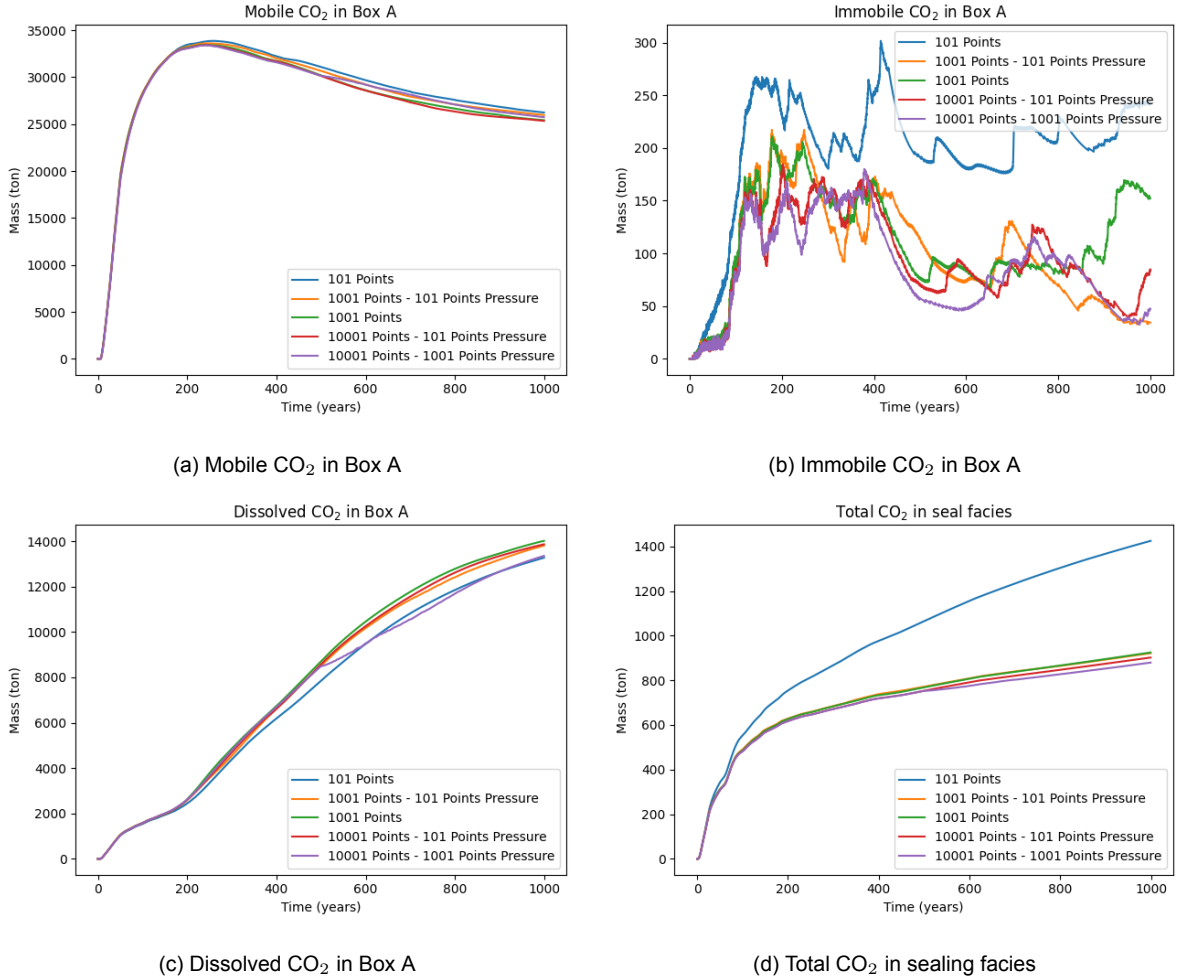

(a) Mobile CO_2 in Box A

(b) Immobile CO_2 in Box A

(c) Dissolved CO_2 in Box A

(d) Total CO_2 in sealing facies

Figure 5.3: Time series data for various OBL resolutions for the CSP reporting grid of 100800 (10 m x 10 m) cells for the 11B case. Curves are labeled with the number of points for all OBL axes not including pressure, and the number of points on the OBL pressure axis. For curves with only one number of points, the discretization is uniform on all three-dimensional axes.

high-resolution models see more fingers as well as clearer, more defined fingers. The low-resolution models see fewer, thicker, and more coarse fingers. This continues into Figure 5.5(b) where the coarse models display larger, coarser fingers than the high-resolution models.

In Figure 5.5(c) within box A, the coarse models display CO_2-rich fingers that are surrounded in brine that is similar in density to the fingers themselves. In the finer models, there is a larger contrast between the density of the fingers and the surrounding brine in addition to both the fingers and the surrounding brine being less dense than their counterparts in the coarse models. This indicates more dissolved CO_2 in the fingers and the surrounding brine in the coarse models.

Similar to when comparing OBL resolutions, using the CSP reporting criteria is useful for comparing grid resolutions. Figure 5.6 shows data for various resolutions of the 11B case. In box A, the two coarser models show lower amounts of mobile CO_2 and higher amounts of dissolved CO_2 relative to the finer models. This reflects the observations in the spatial maps of Figure 5.5. The difference in dissolved CO_2 and mobile CO_2 in box A between the coarse and fine models grows over time after the onset time, but when comparing the 50k model to the 100k model or the 240k model to the 320k model, smaller differences that do not necessarily grow with time are visible. However as the number of cells increases, less CO_2 is dissolved and more CO_2 is mobile.

In box B, fewer correlations can be made. The same general trend of models with more cells having more mobile CO_2 remains in box B, but there is no longer a visible difference between the coarse and fine resolution models. Instead, the 50k and 320k models are outliers. For dissolved CO_2, there is little

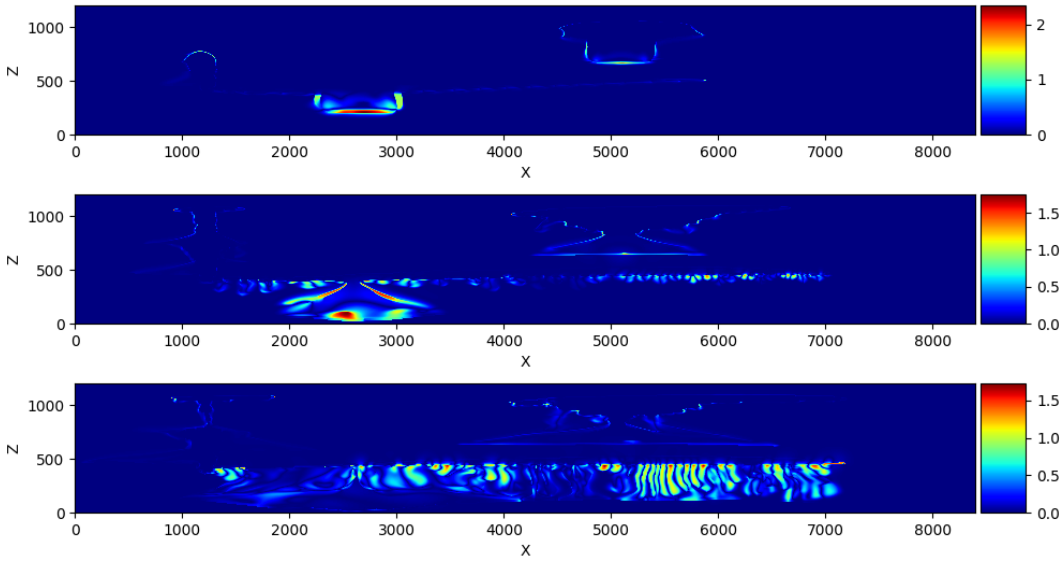

Figure 5.4: Absolute difference (%) in water phase mass density (kg/m^3) for 10001-101 points and 1001-101 points for the CSP reporting grid of 100800 (10 m x 10 m) cells 0, 150, and 450 years after the end of injection.

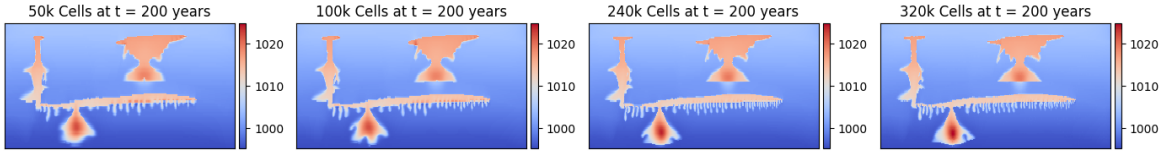

(a) Aqueous phase mass density (kg/m^3) at t = 200 Years

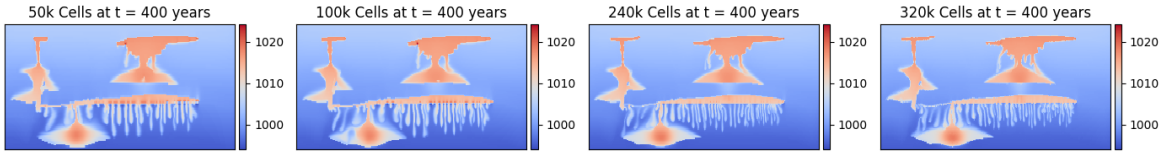

(b) Aqueous phase mass density (kg/m^3) at t = 400 Years

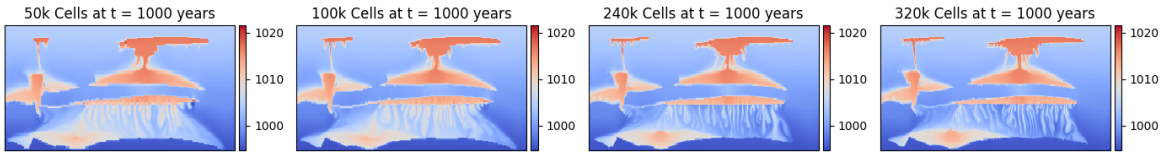

(c) Aqueous phase mass density [kg/m^3] at t = 1000 Years

Figure 5.5: Spatial distribution of CO_2 concentration in brine (kg/m^3) as defined by the CSP for resolutions of 50k (16 m x 12 m), 100k (10 m x 10 m), 240k (7 m x 6 m), and 320k (6.25 m x 5 m) cells, at t = 200 years, t = 400 years, and t = 1000 years. A brine density of 1020 kg/m^3 approximately correlates to a CO_2 mole fraction of 0.027.

variation across all models. Interestingly, the 100k model had the most dissolved CO_2.

Figure 5.6(e) shows convective mixing in box C which is given by

$$M(t) \equiv \int_{Box\ C} \left| \nabla \left(\frac{\chi_c^w}{\chi_{c,max}^w} \right) \right| dV, \tag{5.1}$$

where χ_w^c is the mass-fraction of CO_2 in water and $\chi_w^{c,max}$ is the solubility limit. Convective mixing is heavily reliant on grid size. Increasing grid resolution can increase mixing by orders of magnitude. While all resolutions have similar shapes, finer resolutions result in earlier mixing that is continued

longer into the post-injection phase before eventually reaching an equilibrium level of mixing.

To assess seal quality, the mass of CO_2 in sealing facies (facies 1) within the entire reservoir is shown. As resolution is increased, the mass of CO_2 within seals decreases. Again, a large disparity between the coarse and fine groups of models can be seen. Within these groups, finer grids resulted in less CO_2 in the seals. In all models, the end of the injection period at t = 50 years can be seen as a spike in CO_2 in the sealing layers. This is most pronounced in the finer-resolution models.

Another effective way to visualize trapping mechanisms other than the CSP reporting curves is to look at trapping mechanism contribution plots. Figure 5.7 shows these plots in boxes A and B for different grid resolutions of the 11B case. In all resolutions, residual trapping is effectively not present in box A except for a small period between 100 and 200 years after the end of injection. This is because the CO_2 in this region exists only in the form of a trapped plume and later as of fingers. At the onset time, solubility trapping begins to contribute more to overall trapping due to these fingers. In the coarser models, solubility trapping is more relevant which reflects what was seen in Figure 5.6 where finer resolution models see more realistic (less) CO_2 entering the sealing units.

Once fully formed at the end of injection, the plume in box A does not move and hence does not leave a trail of immobile CO_2. Additionally, there are no facies interfaces in box A other than those of a single permeable sandstone and two sealing facies. This homogeneous environment does little to residually trap CO_2. In box B, there are several facies interfaces that the CO_2 plume crosses as it rises through the box. At every interface and as the plume moves upward, CO_2 is trapped residually. Because of this, all three mechanisms play a role in box B. Behavior differs more among grid resolutions with residual trapping varying most in the 400-600 year post-injection range, but there is no direct correlation between grid size and the relative prevalence of different trapping mechanisms. This is likely related to the plume in box B not being fully developed until very late into the post-injection period. This lack of full development decreases the effectiveness of structural trapping as much of the CO_2 is trapped either residually or via dissolution before reaching the shallowest capillary barrier that acts as a seal for the fully developed plume.

5.2.3. Mass-Rate Approximation

The injection rate during all models was set to a constant mass rate of 3024 kg/day. The rate approximation technique described in chapter 2 was used to emulate injection wells and match this rate. Figure 5.8 shows the average rate per well over time for variations in OBL points and grid cells for the 11B case. From t = 0 to t = 25 years, the rate shown is the rate of Well 1 calculated from the total mass of CO_2 in the reservoir at a given time divided by the current time to get an average rate. From t = 25 to t = 50 years, the plotted values represent the average of Well 1 and Well 2 as it is not possible to differentiate in this technique. The large drop in the average rate at t = 25 years indicates a low initial rate in Well 2, but Well 2 quickly reaches the desired rate. There is no correlation between OBL points or grid resolution and rate. As the defined rate for 11B is 3024 kg/day for each well, the total mass of CO_2 in the reservoir is lower than expected. Before the beginning of injection from Well 2, the % error of both plots is ~0.5% while when both injectors are on, this error is reduced to ~0.2%. Only the 1001 OBL point rate was above this with an error of ~0.4% after t = 25 years.

5.3. 11C Case

The final results for the 11C case are currently a work in progress. While the finalized results are not available for this thesis, this study has laid the groundwork for results to be submitted to the CSP. The CSP reporting grid is 168 x 100 x 120 (50 m x 50 m x 10 m) cells. Any results to be submitted will be at this resolution or a resolution finer than this. To run models of these sizes, a GPU platform is required. Development of this platform for current versions of open-darts is outside the scope of this project but has been completed recently. Unfortunately, there was not enough time to utilize this platform for this study. However, models with coarser resolutions for the 11C case were performed using a CPU platform. Preliminary results can be seen in Figure 5.9 with the top model including 98k cells (3864 in slice) and the bottom model including 767k cells (15300 in slice) being shown at t = 400 years. The resolution is too coarse to see individual fingers, but downward-moving columns of CO_2-saturated brine are visible in both models.

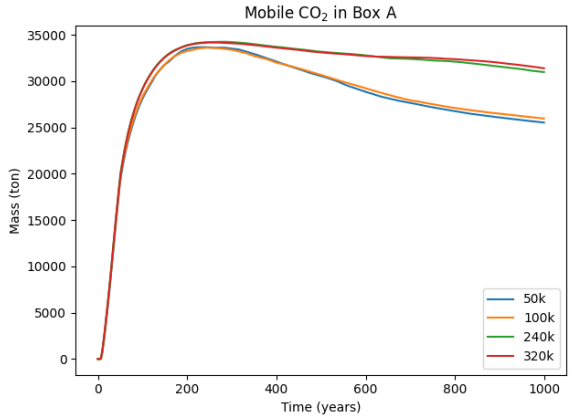

(a) Mobile CO_2 in Box A

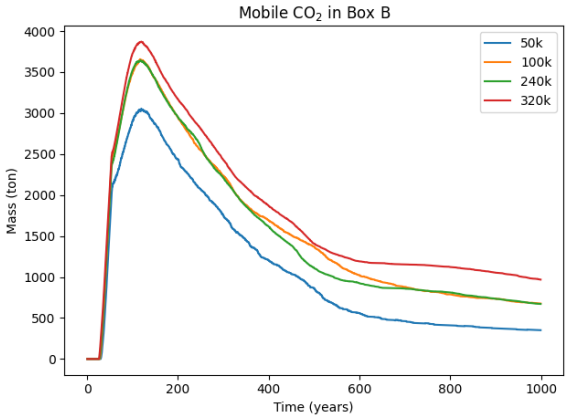

(b) Mobile CO_2 in Box B

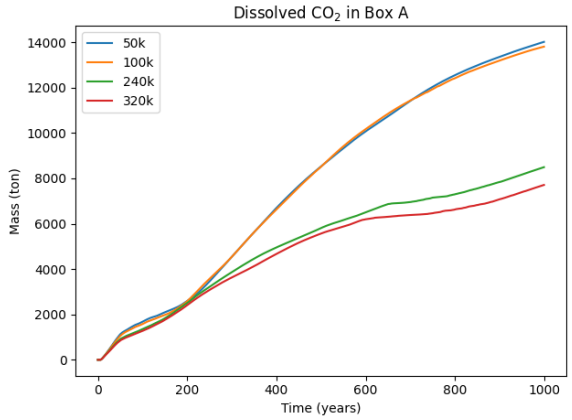

(c) Dissolved CO_2 in box A

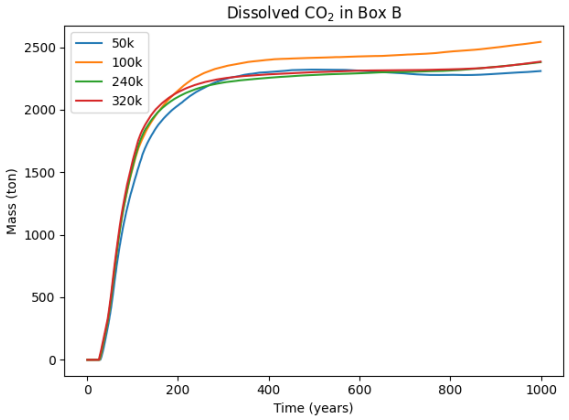

(d) Dissolved CO_2 in box B

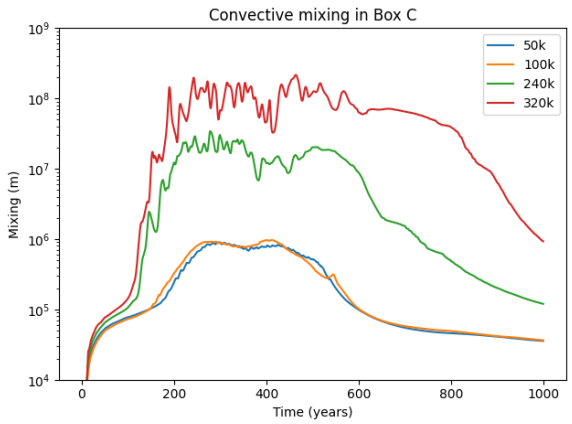

(e) Convective mixing in box C

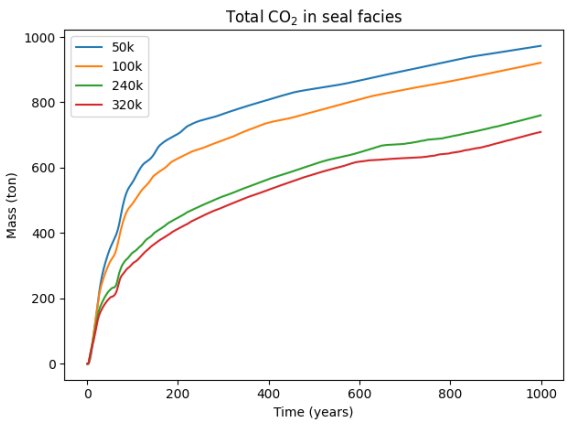

(f) Total CO_2 in sealing facies

Figure 5.6: CSP time series data for grid resolutions of 50k (16 m x 12 m), 100k (10 m x 10 m), 240k (7 m x 6 m), and 320k (6.25 m x 5 m) cells for the 11B case

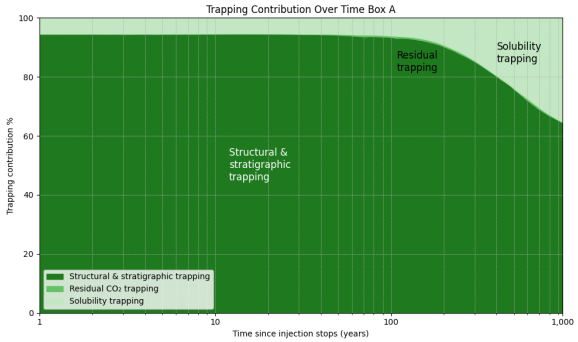

(a) 50k cells Box A

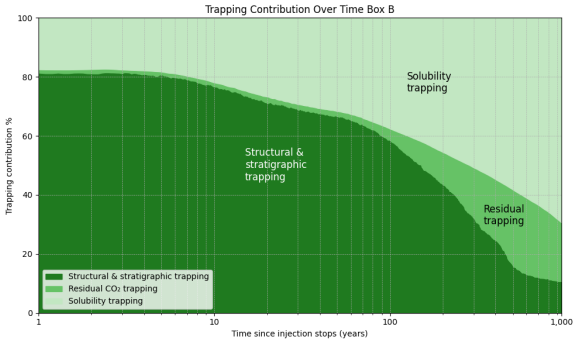

(b) 50k cells Box B

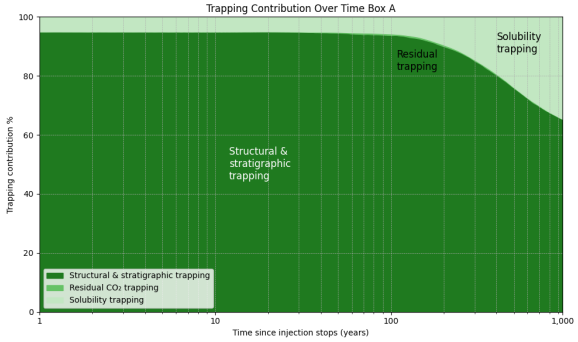

(c) 100k cells Box A

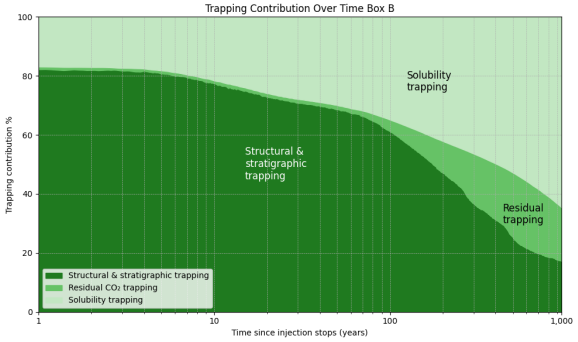

(d) 100k cells Box A

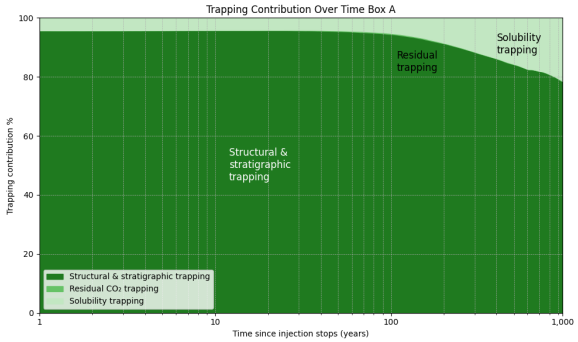

(e) 240k cells Box A

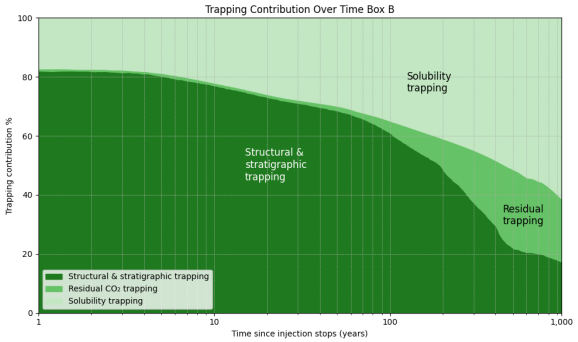

(f) 240k cells Box A

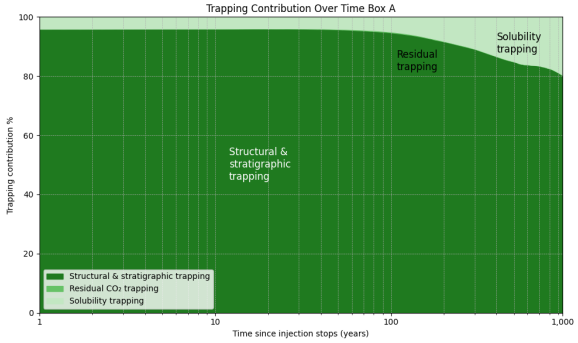

(g) 320k cells Box A

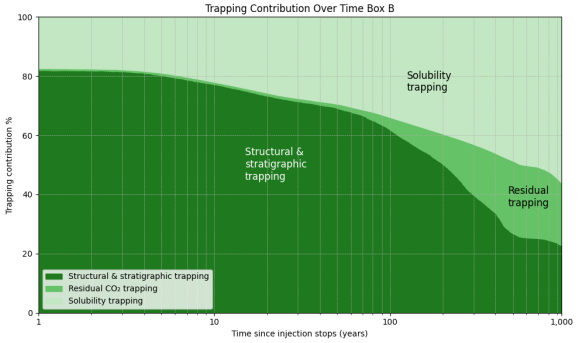

(h) 320k cells Box A

Figure 5.7: Trapping mechanisms over time in Box A and Box B for grid resolutions of 50k (16 m x 12 m), 100k (10 m x 10 m), 240k (7 m x 6 m), and 320k (6.25 m x 5 m) cells in the 11B case

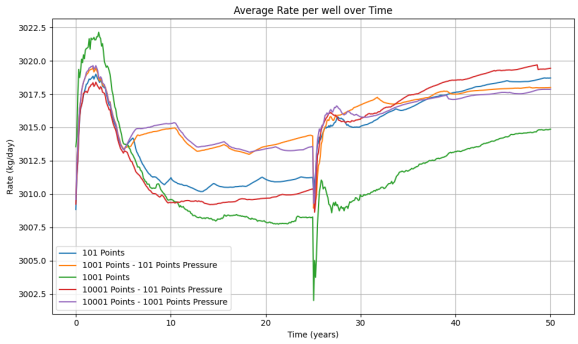

(a) Average injection rate (kg/day) for various OBL resolutions

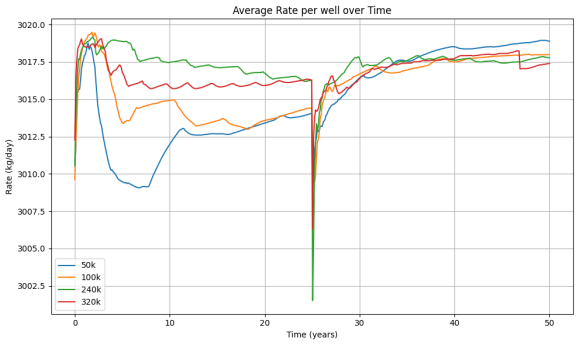

(b) Average injection rate (kg/day) for various grid cell resolutions

Figure 5.8: Average injection rate (kg/day) for various OBL and grid resolutions for 11B case; **a** Various OBL resolutions for the 11B model at the CSP reporting grid of 100800 (10 m x 10 m) cells, and **b** Grid resolutions of 50k (16 m x 12 m), 100k (10 m x 10 m), 240k (7 m x 6 m), and 320k (6.25 m x 5 m) cells for 11B case. From t = 0 to t = 25 years, the rate shown is that of Well 1. From t = 25 to t = 50 years, the rate shown is the average rate of both Well 1 and Well 2

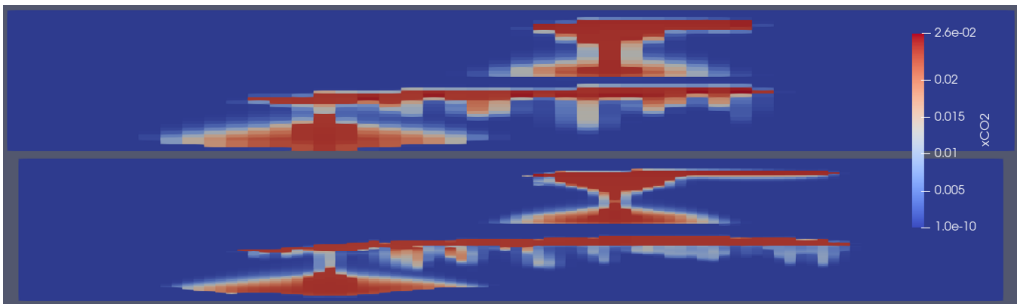

Figure 5.9: Snapshot of 11C case 400 years after the beginning of injection showing CO_2 mole fraction in aqueous phase for models with 98k (top) and 767k (bottom) cells. Slices are taken from the center of the anticline at y = 2500 m and show 3864 ~ (185m x 28.5 m) and 15300 ~ (93 m x 14 m) cells for the top and bottom models respectively. Both models use tetrahedral unstructured grids with irregular cell dimensions.

6

Discussion

Due to challenges at surface conditions, no successful run of the 11A model has yet occurred. The main issues are related to the injected CO_2 that partially ignores the sealing facies and continuously rises in the domain. After a short number of time-steps, the system begins to overpressure as CO_2 below the sealing fault accumulates which results in the pressure of the fault cells increasing in a non-physical manner. One solution would be to deactivate the cells of facies 7 by setting the active number (ACTNUM) to 0. This would solve overpressuring issues, but it would not fix the non-physical behavior that the CO_2 exhibits before reaching the fault such as ignoring geologic boundaries.

The incorrect CO_2 flow is interesting as in the FluidFlower benchmark, open-darts displayed accurate results at surface conditions. A number of differences between the models for SPE11 and FluidFlower could be responsible for inaccurate results for the 11A case. These include but are not limited to different diffusion coefficients of the vapor phase, linear solvers used, or reservoir geometries. It is speculated that the larger diffusion coefficient in SPE11 is a driving factor for the inaccurate behavior observed.

The value given by the CSP for the vapor phase diffusion coefficient is four orders larger than the coefficient for the aqueous phase. This large difference makes capturing realistic behavior challenging when combined with surface conditions. However, this large value has been used and included in many successful simulations from other participating groups of the CSP. Although some improvements are seen after decreasing this value, some issues remain related to diffusion which indicates that the coefficient is not the only factor limiting the accuracy of the model.

A more likely reason for unrealistic behavior is that in open-darts, diffusion is upstream-weighted. Across a capillary boundary where some diffusion is expected, an upstream-weighted system will overestimate the diffusive flux of CO_2 vapor, especially when the diffusion coefficient of vapor is relatively large. This was seen in Figure 5.1 where evidence of CO_2 diffusing through the sealing layer was seen. Capillary entry pressure seems to have some small impact on this process as CO_2 is seen trapped against the impermeable fault, the seal facies, and the two least permeable sand facies, but this effect appears to be dominated by diffusion. If diffusion were calculated using a midstream-weighed average such as an arithmetic average, the diffusive flux would be less likely to be overestimated and more likely to be represented accurately. Making this change is outside the scope of this study, but for the final CSP submission, this change will likely result in strong submissions for the 11A case.

Other than the OBL comparison study, every model in this study used 1001 OBL points with 101 points on the pressure axis. This parametrization was chosen due to the best computational performance while maintaining high accuracy compared to models with more OBL points in the OBL resolution study. Because the resolution study was performed on the 11B case, it is not a guarantee that the 11A and 11C cases should also use a 1001-101 parametrization. For 11C, because the conditions are the same as 11B, a 1001-101 parametrization would likely be sufficient. For the 11A case, surface conditions likely require additional points. A separate OBL resolution study is necessary for surface conditions. This would first require diffusion changes to produce accurate results for the 11A case.

In general, the results from the 11B case are promising for future numerical modeling of GCS, but several points should be discussed. All models run in this study used Cartesian grids. When discretizing with unstructured grids, irregular behavior was observed. Fixing this behavior was outside of the scope of this project and will be investigated in the future. In the structured models, inflow and outflow of CO_2 due to flow or diffusion are not fully smooth due to numerical effects. Although these effects decrease as grid resolution becomes finer, runtime required for more refined models must be considered.

In terms of grid resolution, all four resolutions used were able to capture the effects CO_2 and its fingering behavior. However, based on the curves in Figure 2.6, the critical wavelength of fingers in box A (facies 5) at field conditions should likely be between 6 to 50 cm. This would imply that the results from the 11B case were not numerically converged and did not capture fingering accurately but instead mimicked fingering behavior. This is likely not a good assumption. The Riaz et al. [2006] model is for homogeneous and extremely idealized conditions. Open-darts is validated against analytic solutions like the Riaz et al. [2006] model and has recently performed comparably with an earlier version of open-darts for enhanced dissolution problems. The results for the 11B case can likely be considered numerically converged. Specifically, the two finer resolution models of 240k and 320k cells are most likely fully converged. The large difference between the coarse and fine grids suggests that the coarse resolution is not sufficient. This is supported by the behavior of the fingers in box A for the coarse models in Figure 5.5. If the assumption that the resolution required to converge fingering is between the 100k and 240k models, it would place the critical wavelength between 7 and 10 meters and the penetration depth between 6 and 10 meters. To further support these claims, additional models with cell dimensions in these ranges can be run, analyzed and compared to the 100k and 240k models. To support the idea that we reach convergence, a model with > 1000k cells could be run. Results from a very refined model similar to those of the 240k and 320k models would suggest that these models are already numerically converged.

Similar to 11A, suspected issues with upstream-weighted diffusion had visible effects in 11B. The first of these effects can be seen in Figure 5.3(d) and 5.6(f) where the total mass of CO_2 in sealing facies is shown. Although with more grid cells and to a lesser extent OBL points, CO_2 in the seals is lower, the curves in this study show more CO_2 in seals than what was reported by most other groups at preliminary results meetings for the CSP. The second effect due to suspected upstream-weighting issues was seen in the highly permeable fracture below box B. When the CO_2 plume reaches the fracture after 20-25 years of injection, the plume doesn't follow the fracture up and to the right, but instead continues to travel vertically through less permeable facies seemingly by diffusion. Only much later does the CO_2 follow the fracture. At this point, the plume that ignored the fracture is already hundreds of meters above the tip of the plume furthest in the fracture. The end behavior would likely be similar if the plume had followed the fracture, but for different geometries where open-darts could be used, this may not be the case. In general, these effects were not as pronounced at reservoir scale and conditions with a much lower CO_2 diffusion coefficient compared to surface conditions, but they were still present and had an effect on the output.

The rate approximation technique used in this study was demonstrated to perform well at approximating mass injection rates and replacing wells in the 11B and 11C field-scale cases. Not enough data was collected on the usage of this technique at surface conditions to claim its effectiveness at those conditions. This was important because before the use of this technique, In the 11B and 11C cases, numerous convergence problems related to well objects were encountered before the implementation of this technique. With very low errors throughout all models, the technique can be considered a reliable replacement for wells at field conditions as it was very effective and significantly more efficient. This technique has some complications for replacing production wells, but with property interpolation, production wells can be emulated.

As previously mentioned, the 11C case is a work in progress. To run even the CSP reporting grid of 2000k (50 m x 50 m x 10 m) cells in a reasonable amount of time, a GPU platform is required. For the final CSP submission, a newly updated GPU platform can be used with the existing 11C case model to directly create results that can be submitted. When looking at Figure 5.9, the current results for the 11C case are promising. Unlike the 11B case, no CO_2 reaches the spill point to the left of Well 1 to eventually enter box B. This is because the plume moves along the y direction (into and out of Figure 5.9) along the arch of the 3D reservoir. Plume movement to the right of Well 1 is similar to that of the

11B case and dense columns of CO_2 are seen sinking. These resolutions are much more coarse than the 50k and 100k models in the 11B case, and as such are not converged solutions. To achieve a converged solution, grid cell size must be at least finer than 10 m x 10 m x 10 m. This would require at least 50.4 million cells if a uniform Cartesian grid is used. Solutions to this problem for future models could include localized grid refinement or enhanced dissolution upscaling technique similar to what was used in a study by Lyu and Voskov [2023].

To contribute to a reference case for the numerical simulation of GCS, this study has shown results that are very relevant both to numerical simulation, but also to actual GCS projects. The heterogeneous geometry defined by the benchmark organizers includes realistic structures such as fractures and faults. The behavior seen in numerical models around these features can be used to better understand and predict CO_2 plume behavior around these same types of features in real reservoirs. In terms of realistic seal integrity, the understanding of upstream-weighted diffusion and its overestimation can be used to better assess containment risk.

The CSP omitted several phenomena in the benchmark. For example, geologic heterogeneity was included only on a large scale. Within a facies, properties were homogeneous. Although this was a choice to allow for better comparison between groups and to better understand the effects of large-scale heterogeneities, it is still a large assumption. Further studies with heterogeneous rock properties within facies can be performed on this same geometry to compare and analyze the effects of small-scale heterogeneities. Future models can include the effects of hysteresis related to relative permeability and capillary pressure which were not considered in the CSP.

One of the largest assumptions was the non-inclusion of the effects of salinity. Modeling this requires a compositional simulator of which open-darts is one. Black oil simulators, used by some participating groups in the CSP, are incapable of including salinity, so it was omitted. However, for this study, attempts were made to include constant molality for the 11B case with 240k cells. This was aimed at quantifying the effects of realistic salinity on plume migration and diffusive fingering as with increasing salinity, the amount of CO_2 that can be dissolved decreases. Unfortunately, the required changes to darts-flash were not completed in time to perform a full study.

The CSP also assumed an injection stream of pure CO_2. In reality, there will be impurities in the stream such as C1 or H2S. Three component models using H_2O, CO_2, and 5 mol% of either C1 or H2S were ran on the 11B case 240k cell model. For the three component models, the built-in composition correction was over-correcting in every cell and altering the overall composition. Because of this, the three component models were abandoned for this report.

7

Conclusion

In this study, open-darts and its accompanying thermodynamic library darts-flash utilized advanced numerical modeling techniques to participate and produce results for the 11th Society of Petroleum Engineers Comparative Solution Project. The complex behavior of the CO_2-brine system was represented with a fugacity-activity model with CO_2 dissolution. The highly nonlinear problems were solved using the Operator-Based Linearization (OBL) method. An adjusted injection rate approximation method was used to accurately represent CO_2 mass injection as a residual correction. An iterative linear solver using the FGMRES method with a two-step CPR preconditioner was used. A time-stepping strategy that bases the next time-step multiplier on maximum changes of state variables in the reservoir was used. Sensitivity analyses were performed on OBL resolution and grid cell resolution for the 11B case to determine the number of OBL points necessary to accurately show CO_2-brine behavior and to see the effects of refinement on important factors such as fingering behavior and seal integrity.

Bibliography

Summary for Policymakers, page 3–48. Cambridge University Press, 2023.

Halidi Abdoulghafour, Mohammad Sarmadivaleh, Lars Petter Hauge, Martin Fernø, and Stefan Iglauer. Capillary pressure characteristics of co2-brine-sandstone systems. *International Journal of Greenhouse Gas Control*, 94:102876, 2020.

Temitope Ajayi, Adedapo Awolayo, Jorge S Gomes, Humberto Parra, and Jialiang Hu. Large scale modeling and assessment of the feasibility of co2 storage onshore abu dhabi. *Energy*, 185:653–670, 2019.

K. Aziz and A. Settari. Petroleum reservoir simulation. *Applied Science Publishers*, 476, 1979. URL https://cir.nii.ac.jp/crid/1573950398841360000.

Shigeru Bando, Fumio Takemura, Masahiro Nishio, Eiji Hihara, and Makoto Akai. Viscosity of aqueous nacl solutions with dissolved co2 at (30 to 60) °c and (10 to 20) mpa. *Journal of Chemical & Engineering Data*, 49(5):1328–1332, 2004. doi: 10.1021/je049940f. URL https://doi.org/10.1021/je049940f.

A Behie and P Forsyth Jr. Comparison of fast iterative methods for symmetric systems. *IMA Journal of Numerical Analysis*, 3(1):41–63, 1983.

Mojdeh Delshad, Xianhui Kong, Reza Tavakoli, Seyyed A Hosseini, and Mary F Wheeler. Modeling and simulation of carbon sequestration at cranfield incorporating new physical models. *International Journal of Greenhouse Gas Control*, 18:463–473, 2013.

M.T. Elenius, D.V. Voskov, and H.A. Tchelepi. Interactions between gravity currents and convective dissolution. *Advances in Water Resources*, 83:77–88, 2015. ISSN 0309-1708. doi: https://doi.org/10.1016/j.advwatres.2015.05.006. URL https://www.sciencedirect.com/science/article/pii/S0309170815000998.

Yaqing Fan, Louis J Durlofsky, and Hamdi A Tchelepi. A fully-coupled flow-reactive-transport formulation based on element conservation, with application to co□ storage simulations. 2012.

A. Fenghour, William A. Wakeham, and V. Vesovic. The Viscosity of Carbon Dioxide. *Journal of Physical and Chemical Reference Data*, 27(1):31–44, 01 1998. ISSN 0047-2689. doi: 10.1063/1.556013. URL https://doi.org/10.1063/1.556013.

MA Fernø, Malin Haugen, Kristoffer Eikehaug, Olav Folkvord, Benyamine Benali, Jakub W Both, Erlend Storvik, Casey W Nixon, Robert L Gawthrope, and Jan Martin Nordbotten. Room-scale co2 injections in a physical reservoir model with faults. *Transport in Porous Media*, 151(5):913–937, 2024.

Bernd Flemisch, Jan M Nordbotten, Martin Fernø, Ruben Juanes, Jakub W Both, Holger Class, Mojdeh Delshad, Florian Doster, Jonathan Ennis-King, Jacques Franc, et al. The fluidflower validation benchmark study for the storage of co 2. *Transport in Porous Media*, pages 1–48, 2023.

Julio E Garcia. Density of aqueous solutions of co2. 2001.

Laura Grigori, James W Demmel, and Xiaoye S Li. Parallel symbolic factorization for sparse lu with static pivoting. *SIAM Journal on Scientific Computing*, 29(3):1289–1314, 2007.

Lubomir Hnědkovský, Robert H. Wood, and Vladimir Majer. Volumes of aqueous solutions of ch4, co2, h2s and nh3at temperatures from 298.15 k to 705 k and pressures to 35 mpa. *The Journal of Chemical Thermodynamics*, 28(2):125–142, 1996. ISSN 0021-9614. doi: https://doi.org/10.1006/jcht.1996.0011. URL https://www.sciencedirect.com/science/article/pii/S0021961496900117.

Akand W Islam and Eric S Carlson. Viscosity models and effects of dissolved co2. *Energy & fuels*, 26 (8):5330–5336, 2012.

Mark Khait and Denis V. Voskov. Operator-based linearization for general purpose reservoir simulation. *Journal of Petroleum Science and Engineering*, 157:990–998, 2017. ISSN 0920-4105. doi: https://doi.org/10.1016/j.petrol.2017.08.009. URL https://www.sciencedirect.com/science/article/pii/S0920410516310907.

Diana Koschel, Jean-Yves Coxam, Laurence Rodier, and Vladimir Majer. Enthalpy and solubility data of co2 in water and nacl (aq) at conditions of interest for geological sequestration. *Fluid phase equilibria*, 247(1-2):107–120, 2006.

EW Lemmon, IH Bell, ML Huber, and MO McLinden. Thermophysical properties of fluid systems in nist chemistry web-book, nist standard reference database (2023), 2023.

Xiaocong Lyu and Denis Voskov. Advanced modeling of enhanced co2 dissolution trapping in saline aquifers. *International Journal of Greenhouse Gas Control*, 127:103907, 2023. ISSN 1750-5836. doi: https://doi.org/10.1016/j.ijggc.2023.103907. URL https://www.sciencedirect.com/science/article/pii/S1750583623000774.

Michael L. Michelsen. The isothermal flash problem. part ii. phase split calculation. *Fluid Phase Equilibria*, 9:21–40, 1982. doi: 10.1016/0378-3812(82)85002-4.

Michael L Michelsen and Jørgen M Mollerup. *Thermodynamic models: fundamentals & computational aspects*. Tie-Line Publications Holte, Denmark, 2004.

Jan M Nordbotten, Bernd Flemisch, SE Gasda, HM Nilsen, Yaqing Fan, Gillian Elizabeth Pickup, Bernd Wiese, Michael Anthony Celia, HK Dahle, GT Eigestad, et al. Uncertainties in practical simulation of co2 storage. *International Journal of Greenhouse Gas Control*, 9:234–242, 2012.

Jan M Nordbotten, Martin Fernø, Bernd Flemisch, Ruben Juanes, and Magne Jørgensen. Experimentally assessing the uncertainty of forecasts of geological carbon storage. *International Journal of Greenhouse Gas Control*, 135:104162, 2024a.

Jan M. Nordbotten, Martin A. Ferno, Bernd Flemisch, Anthony R. Kovscek, and Knut-Andreas Lie. The 11th Society of Petroleum Engineers Comparative Solution Project: Problem Definition. *SPE Journal*, pages 1–18, 01 2024b.

JM Nordbotten, M Fernø, B Flemisch, R Juanes, and M Jørgensen. Final benchmark description: fluidflower international benchmark study.(2022).

Ding-Yu Peng and Donald B Robinson. A new two-constant equation of state. *Industrial & Engineering Chemistry Fundamentals*, 15(1):59–64, 1976.

Karsten Pruess and Jan Nordbotten. Numerical simulation studies of the long-term evolution of a co 2 plume in a saline aquifer with a sloping caprock. *Transport in porous media*, 90:135–151, 2011.

A Riaz, M Hesse, HA Tchelepi, and FM Orr. Onset of convection in a gravitationally unstable diffusive boundary layer in porous media. *Journal of Fluid Mechanics*, 548:87–111, 2006.

Philip Ringrose. How to store co2 underground: Insights from early-mover ccs projects. 2020.

Youcef Saad. A flexible inner-outer preconditioned gmres algorithm. *SIAM Journal on Scientific Computing*, 14(2):461–469, 1993.

Nicolas Spycher, Karsten Pruess, and Jonathan Ennis-King. Co2-h2o mixtures in the geological sequestration of co2. i. assessment and calculation of mutual solubilities from 12 to 100°c and up to 600 bar. *Geochimica et Cosmochimica Acta*, 67(16):3015–3031, 2003. ISSN 0016-7037. doi: https://doi.org/10.1016/S0016-7037(03)00273-4. URL https://www.sciencedirect.com/science/article/pii/S0016703703002734.

Klaus Stüben. Algebraic multigrid (amg): experiences and comparisons. *Applied mathematics and computation*, 13(3-4):419–451, 1983.

Denis V. Voskov. Operator-based linearization approach for modeling of multiphase multi-component flow in porous media. *Journal of Computational Physics*, 337:275–288, 2017. ISSN 0021-9991. doi: https://doi.org/10.1016/j.jcp.2017.02.041. URL https://www.sciencedirect.com/science/article/pii/S0021999117301444.

John Richard Wallis. Incomplete gaussian elimination as a preconditioning for generalized conjugate gradient acceleration. In *SPE Reservoir Simulation Conference?*, pages SPE–12265. SPE, 1983.

John Richard Wallis, Richard P Kendall, and TE Little. Constrained residual acceleration of conjugate residual methods. In *SPE Reservoir Simulation Conference?*, pages SPE–13536. SPE, 1985.

Michiel Wapperom, Xiaoming Tian, Aleks Novikov, and Denis Voskov. Fluidflower benchmark: Lessons learned from the perspective of subsurface simulation. *Transport in Porous Media*, pages 1–20, 2023.

Zaman Ziabakhsh-Ganji and Henk Kooi. An equation of state for thermodynamic equilibrium of gas mixtures and brines to allow simulation of the effects of impurities in subsurface co2 storage. *International Journal of Greenhouse Gas Control*, 11:S21–S34, 2012. ISSN 1750-5836. doi: https://doi.org/10.1016/j.ijggc.2012.07.025. URL https://www.sciencedirect.com/science/article/pii/S175058361200182X. CATO: CCS Research in the Netherlands.